JOURNAL OF GEOPHYSICAL RESEARCH: SOLID EARTH, VOL. 118, 1–19, doi:10.1002/2013JB010529, 2013

Aftershocks of the 2010 M_w 7.2 El Mayor-Cucapah earthquake reveal complex faulting in the Yuha Desert, California

Kayla A. Kroll,[1] Elizabeth S. Cochran,[2] Keith B. Richards-Dinger,[1] and Danielle F. Sumy[2]

Received 18 July 2013; revised 14 October 2013; accepted 16 October 2013.

[1] We detect and precisely locate over 9500 aftershocks that occurred in the Yuha Desert region during a 2 month period following the 4 April 2010 M_w 7.2 El Mayor-Cucapah (EMC) earthquake. Events are relocated using a series of absolute and relative relocation procedures that include Hypoinverse, Velest, and hypoDD. Location errors are reduced to ∼40 m horizontally and ∼120 m vertically. Aftershock locations reveal a complex pattern of faulting with en echelon fault segments trending toward the northwest, approximately parallel to the North American-Pacific plate boundary and en echelon, conjugate features trending to the northeast. The relocated seismicity is highly correlated with published surface mapping of faults that experienced triggered surface slip in response to the EMC main shock. Aftershocks occurred between 2 km and 11 km depths, consistent with previous studies of seismogenic thickness in the region. Three-dimensional analysis reveals individual and intersecting fault planes that are limited in their along-strike length. These fault planes remain distinct structures at depth, indicative of conjugate faulting, and do not appear to coalesce onto a throughgoing fault segment. We observe a complex spatiotemporal migration of aftershocks, with seismicity that jumps between individual fault segments that are active for only a few days to weeks. Aftershock rates are roughly consistent with the expected earthquake production rates of Dieterich (1994). The conjugate pattern of faulting and nonuniform aftershock migration patterns suggest that strain in the Yuha Desert is being accommodated in a complex manner.

Citation: Kroll, K. A., E. S. Cochran, K. B. Richards-Dinger, and D. F. Sumy (2013), Aftershocks of the 2010 M_w 7.2 El Mayor-Cucapah earthquake reveal complex faulting in the Yuha Desert, California, *J. Geophys. Res. Solid Earth*, *118*, doi:10.1002/2013JB010529.

1. Introduction

[2] Precise relocation of seismicity can be used to image fault structures across the seismogenic zone. The 4 April 2010 M_w 7.2 El Mayor-Cucapah (EMC) earthquake produced a vigorous cloud of aftershocks approximately 4 km northwest of the main shock rupture termination in the Yuha Desert. The Yuha Desert is a region of complex faulting between the Laguna Salada fault zone to the south and Elsinore Fault zone to the north (Figure 1) and is located just north of the California-Mexico border and approximately 30 km west of Calexico, California. The Laguna Salada fault extends from the Sierra Cucapah range in Baja California, northwestward toward the U.S.-Mexico border and terminates in the Yuha Desert. Previous studies suggest that the Laguna Salada fault system initiated after the formation of the San Andreas Fault, located approximately 75 km to the east, during a period of late Quaternary wrench deformation [*Crowell*, 1978; *Dokka and Merriam*, 1982; *Mueller*, 1984; *Pinault and Rockwell*, 1984; *Isaac*, 1987]. They report primarily right-lateral strike-slip motion with a smaller component of normal slip along the Laguna Salada.

[3] Some studies suggest that the Elsinore Fault is the northward extension of the Laguna Salada fault owing to its location, northwest orientation, and slip rate [e.g., *Fuis and Kohler*, 1984; *Mueller and Rockwell*, 1995; *Magistrale and Rockwell*, 1996]. Along its northern extent, the Elsinore Fault is mapped as a fairly simple, single strand, whereas in the south it splays into two strands, the Elsinore Fault to the west and the Agua Tibia-Earthquake Valley (ATEV) fault to the east [*Magistrale and Rockwell*, 1996]. Slip is partitioned between these two fault strands with slip rate estimates of 5 to 6 mm/yr on the Elsinore and 0.5 to 2.8 mm/yr on the ATEV faults [*Magistrale and Rockwell*, 1996]. The Elsinore Fault is mapped further south, past the Coyote Mountains, ∼5 km northwest of the Yuha Desert [*Rymer et al.*, 2011]. Seismicity indicates that the seismogenic depth along the Elsinore Fault decreases toward the south, with depths of ∼17 km in the north and ∼10 km in the south, due to

Additional supporting information may be found in the online version of this article.

[1]Department of Earth Sciences, University of California, Riverside, California, USA.

[2]United States Geological Survey, Pasadena, California, USA.

Corresponding author: K. A. Kroll, Department of Earth Sciences, University of California, Riverside-Geology Building, 900 University Ave, Riverside, CA 92521, USA. (kkrol001@ucr.edu)

2169-9313/13/10.1002/2013JB010529

a steeper geothermal gradient as extension in the Salton Trough is approached [*Magistrale and Rockwell*, 1996].

[4] Faults in the Yuha Desert region link the Elsinore Fault to the northwest and the Laguna Salada fault to the south-southeast, with geologic surface mapping suggesting that the region is underlain by a zone of complex faulting [*Dibblee*, 1954; *Isaac*, 1987]. *Isaac* [1987] mapped both northwest trending right-lateral and northeast trending left-lateral strike-slip faults, with sporadic north-south trending faults displaying normal offset. The primary structure in the Yuha Desert is the Laguna Salada fault which exhibits anastomosing behavior. The main branches in the region are the Laguna Salada-West branch (LS-W) and the Laguna Salada-East branch (LS-E) which exist as separate strands from the Yuha Desert to 1 km south of the California-Mexico border [*Isaac*, 1987]. *Isaac* [1987] also mapped multiple horsetail fractures at the northern end of the LS-E branch. All branches of the Laguna Salada are mapped as dipping steeply to the west at angles between 52° and 90°. *Rymer et al.* [2011] suggest that shallow faults in this area are bounded by a complex system of folds with axes trending dominantly toward the northeast and rotating clockwise approaching the Laguna Salada fault zone that was originally mapped by *Isaac* [1987].

[5] While the surface mapping suggests a complex set of faults in the Yuha Desert, it is unclear whether these structures extend to depth. Previous studies suggest that complex surface faulting may become simpler at depth as faults coalesce onto prominent structures, so-called flower structures [*Weldon II et al.*, 2002; *Bozkurt and Koçyiôit*, 1996; *Wei et al.*, 2011]. Active flower structures have been observed along major well-developed strike-slip fault systems such as the southern San Andreas fault [*Weldon II et al.*, 2002], along other major strike-slip fault systems in Southern California [*Harding*, 1985, 1988; *Dooley and McClay*, 1996], and along the North Anatolian fault [*Bozkurt and Koçyiôit*, 1996]. Conversely, it has also been shown that highly active, immature strike-slip fault systems may consist of parallel throughgoing fault strands, with secondary splays at varying orientations [*Rybicki*, 1973; *Segall and Pollard*, 1980; *Reasenberg and Ellsworth*, 1982]. The San Jacinto fault zone is a prime example of this type of complex, conjugate fault system, where geologic and geophysical data suggest that fault strands remain distinct across the entire seismogenic zone [*Sharp*, 1967].

[6] Earthquake relocations in the Yuha Desert between 1981 and 2010 by *Hauksson et al.* [2002] show seismicity was generally distributed in isolated clusters along northwest trending faults near the mapped trace of the LS-W. Two linear north-northeast trending features are observed in the background seismicity to the northeast of the LS-E branch. However, the limited background seismicity is not sufficient to fully investigate the fault structures. In addition, the aftershock rates and spatiotemporal distribution can provide insights into the stress changes induced by a large main shock [*Omori*, 1894; *King et al.*, 1994; *Toda et al.*, 2005], aftershock rates and migration patterns [*Dieterich*, 1994; *Helmstetter et al.*, 2003], and postseismic deformation [*Hill et al.*, 1993; *Peng and Zhao*, 2009]. Expansion of aftershocks away from the epicenter with time has been observed and may reflect nonuniform (in both space and time) stress changes following an instantaneous stress increase/decrease [*Dieterich*, 1994; *Tajima and Kanamori*, 1985] or perhaps post-seismic deformation and afterslip [*Perfettini and Avouac*, 2004]. However, in areas where no continuous fault structures exist, seismicity may exhibit a more complex spatiotemporal response to the stress changes induced by the main shock.

[7] The work presented here involves the relocation of aftershock hypocenters through a series of absolute and relative relocation steps using the Hypoinverse [*Klein*, 2002], Velest [*Kissling et al.*, 1994] and hypoDD [*Waldhauser and Ellsworth*, 2000]. Precise aftershock locations enable the examination of the intricate network of faults in the Yuha Desert region. We compare the relocated seismicity with the EMC surface offsets mapped by *Rymer et al.* [2011] and with faults previously mapped by *Dibblee* [1954] and *Isaac* [1987] and determine whether the complex faulting seen at the surface extends to depth. Additionally, we investigate the spatiotemporal distribution of aftershocks and aftershock production rates within the region.

2. El Mayor-Cucapah Main Shock

[8] The 4 April 2010 M_w 7.2 El Mayor-Cucapah (EMC) earthquake ruptured multiple fault strands within a complex plate boundary zone (Figure 1) [*Hauksson et al.*, 2010]. The epicenter was located in an area that connects the major right-lateral strike-slip fault systems in California (San Andreas, San Jacinto, and Elsinore Faults) to the spreading center regime in the Gulf of California [*Wei et al.*, 2011]. The EMC is thought to be the largest earthquake on this section of the North American-Pacific plate boundary zone since the 23 February 1892 Laguna Salada earthquake. The Laguna Salada event was estimated to be greater than M_w 7.1 based on the length of surface rupture (at least 22 km of the oblique-dextral section of the Laguna Salada fault and linked Cañon Rojo fault) and the amount of displacement (4 and 3 m of dextral and normal slip, respectively) [*Mueller and Rockwell*, 1995]. The EMC main shock was preceded by a smaller, normal faulting event that occurred about 15 s prior to the main rupture [*Hauksson et al.*, 2010; *Wei et al.*, 2011]. The main shock ruptured bilaterally, ∼55 km to the southeast toward the Gulf of California, with mostly dextral strike-slip motion, and ∼65 km northwestward on multiple fault segments with both normal (eastside down) and dextral motions. *Fletcher et al.* [2010] mapped ∼120 km of surface rupture in the Baja California region and reported up to ∼2.5 m of right-lateral surface slip. Remote-sensing techniques also reveal an average of ∼2 m of right-lateral surface slip in this area, and slip inversions revealed up to 6 m of slip along the fault planes at depth [*Wei et al.*, 2011].

[9] The northwestward rupture propagation ceased ∼5 km south-southeast of the U.S.-Mexico international border in the Yuha Desert. Rupture is not thought to have propagated into the Yuha Desert but rather triggered surface slip on faults therein [*Rymer et al.*, 2011]. *Rymer et al.* [2011] define triggered surface slip as shallow slip occurring on faults remote to the epicenter location. For the purposes of this work, we adopt the interpretation and terminology of *Rymer et al.* [2011] and refer to slip on faults in the Yuha Desert as "triggered surface slip" rather than "coseismic slip." Triggered fault slip was also documented in the Salton Trough (e.g., Coyote Creek Fault, Superstition Hills Fault,

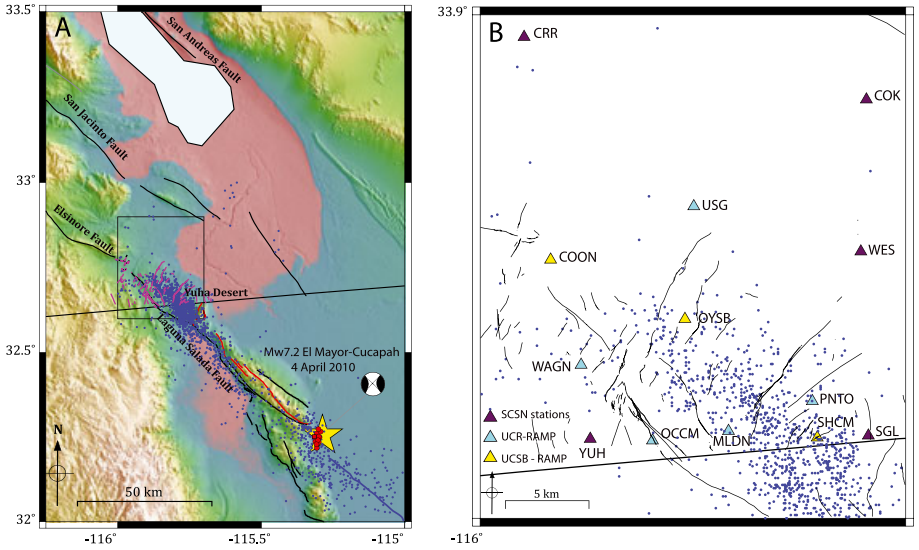

Figure 1. (a) Foreshocks (red circles), the hypocenter of the El Mayor-Cucapah main shock (yellow star), and aftershocks recorded by the Southern California Seismic Network (blue circles) by 6 April 2010. The bilateral main shock surface rupture is shown by the blue (SE rupture) and red (NW rupture) lines, respectively. Faults in the Yuha Desert that exhibit triggered surface slip are shown in magenta [*Rymer et al.*, 2011]. Two main aftershock clusters formed within the 2 days following the main shock, one in the southeast near the epicenter (yellow star) and the second in the Yuha Desert region, north of the international border. (b) An enlarged picture (black box in Figure 1a) showing activated faults and aftershocks that occurred in the Yuha Desert region following the EMC and before the installation of the UC-RAMP stations (triangles) by 6 April 2010.

and Imperial Fault, as well as the Mecca Hills segment of the San Andreas Fault) and surrounding regions including the Yuha Desert (primarily along the Laguna Salada-West branch (LS-W) and Laguna Salada-East branch (LS-E), Yuha Fault, and Yuha Well Fault Zone), between 60 and 172 km north of the epicenter by *Rymer et al.* [2011].

3. Data

[10] To better constrain aftershock locations in the Yuha Desert, an array of eight temporary seismometers were installed as part of the University of California Rapid Aftershock Mobilization Project (UC-RAMP) to supplement the permanent Southern California Seismic Network (SCSN) (Figure 1). The SCSN stations near the Yuha Desert include four short-period stations (COK, CRR, SGL, and YUH) and one continuous broadband station (WES) with broadband and strong motion sensors. Table 1 contains information about the stations used in this study. The eight stations (COON, MLDN, OCCM, OYSB, PNTO, SHCM, USG, and WAGN) of the UC-RAMP array included six portable REFTEK and two Quanterra 330 recording systems with eight L4 sensors (weak motion), seven episensors (strong motion), and one FBA23 sensor (strong motion). The UC-RAMP array was installed above a cluster of aftershocks that was apparent within the first 2 days after the EMC main shock (Figure 1). Three UC-RAMP stations, COON, OYSB, and SHCM, were removed on 15 May 2010, while the remaining stations were installed until 14 June 2010. During the 2 month deployment, the Southern California Seismic Network (SCSN) cataloged 4323 aftershocks within the 20 by 14 km study area (32.63°N, –115.95°E to 32.73°N, –115.75°E).

Table 1. Seismic Station Information[a]

Station Name	Network	Component	Sample Rate (sps)
COK	CI	EHZ	100
CRR	CI	EHZ	100
SGL	CI	EHZ	100
WES	CI	BH[Z,N,E][b], HH[Z,N,E], HN[Z,N,E]	40
YUH	CI	EHZ	100
COON	ZY	EH[Z,N,E][b] HN[Z,N,E]	200
MLDN	ZY	EH[Z,N,E][b] HN[Z,N,E]	100
OCCM	ZY	EH[Z,N,E][b] HN[Z,N,E]	100
OYSB	ZY	EH[Z,N,E][b] HN[Z,N,E]	100
PNTO	ZY	EH[Z,N,E][b] HN[Z,N,E]	100
SHCM	ZY	EH[Z,N,E][b] HN[Z,N,E]	100
USG	ZY	EH[Z,N,E][b] HN[Z,N,E]	100
WAGN	ZY	EH[Z,N,E][b] HN[Z,N,E]	100

[a]CI = SCSN network code, ZY = UC-RAMP network code. EH[Z,N,E] sensors are short period, strong motion accelerometers, HN[Z,N,E] are weak motion sensors, BH[Z,N,E] components are continuous broadband, HH[Z,N,E] are triggered high broadband, and the HN[Z,N,E] sensor at WES is a triggered high broadband accelerometer. The component codes Z, N, and E represent the vertical, north (horizontal), and east (horizontal) directions, respectively. The sample rate is only reported for sensors used in this study.

[b]Data from these sensors were used when multiple sensor data were available at the same site.

4. Relocation Procedure

[11] Routine earthquake locations generated by regional seismic networks often use phase arrivals manually identified by an analyst. However, following large earthquakes, seismic networks often become inundated with aftershock activity, making manual phase picking too laborious and time consuming to be completed in real time. Therefore, in these situations, it is common for locations to be derived from automatically detected phase arrivals, resulting in larger errors [e.g., *Wald et al.*, 1995; *Shearer*, 1997; *Bormann*, 2012]. Thus, it can be difficult to infer fault features as the seismicity tends to have poorly constrained, diffuse locations.

[12] The initial SCSN catalog locations were determined with primarily automatically detected phase arrivals and a layered 1-D velocity model to locate the events with Hypoinverse [*Klein*, 2002]. The SCSN uses a velocity model similar to *Hadley and Kanamori* [1977] for Southern California [e.g., *Wald et al.*, 1995; *Shearer*, 1997; *Wald and Scharwz*, 2000; *Shearer et al.*, 2005; *Hauksson and Shearer*, 2005; *Hutton et al.*, 2006]. The mean horizontal and vertical location errors and root mean square (RMS) traveltime residuals of the events reported in the SCSN catalog are 1.89 km, 2.59 km, and 0.36 s, respectively. Location errors are known to be larger in this area of the Imperial Valley because of the deep sedimentary units [*Fuis and Kohler*, 1984; *Shearer et al.*, 2005; *Hauksson and Shearer*, 2005]. Additional uncertainties in earthquake locations in the Yuha Desert are attributed to inadequate azimuthal station coverage along the southern edge of the network, near the California-Mexico border.

[13] To accurately characterize the fault structure in the Yuha Desert, we undertake a relocation analysis of seismic events recorded by the SCSN and the temporary UC-RAMP stations. We manually pick the phase arrivals for all events in the SCSN catalog within the study area, and we detect additional events in the continuous data recorded by the UC-RAMP array with the Antelope v. 5.1-64 software distributed by Boulder Real Time Technologies (BRTT). Using the phase arrivals, we employ a hierarchical analysis to invert for the best fitting 1-D velocity model and corresponding station corrections for our station and event distribution with Velest [*Kissling et al.*, 1994]. Next we determine individual absolute locations with Hypoinverse [*Klein*, 2002] and lastly apply the double-difference relative relocation algorithm, hypoDD [*Waldhauser and Ellsworth*, 2000], with the refined velocity model to further improve the hypocentral locations and obtain a high-resolution image of seismicity in the Yuha Desert. Detailed processing steps are described in Appendix A.

5. Relocation Results

[14] To improve the resolution of the absolute locations, we employ the double-difference algorithm, hypoDD [*Waldhauser and Ellsworth*, 2000]. hypoDD refines the event locations through an iterative least-squares approach that reduces the differential traveltime residual between pairs of events recorded at a common station. hypoDD assumes that rays from a closely spaced pair of events measured at a common station travel similar paths; therefore, the traveltime difference between the ray pair at a common station is due to the spatial offset between the two earthquakes. This assumption is valid, provided that the event-pair separation distance is small compared to the length scale of the velocity heterogeneities. The algorithm then iteratively adjusts the vector distance between the event pair to reduce the double-difference traveltime residual, resulting in a "relative" location of the event pair. The term "relative" simply implies that each event is located relative to its closest neighbors.

[15] For the final locations, we begin with the hypocenters from Hypoinverse, a 1-D layered velocity model, and combine both the manually and automatically picked traveltimes (404,090 *P*-phase and 251,610 *S*-phase differential times) and 1,629,485 *P*-phase and 1,511,309 *S*-phase cross-correlation delay times. We successfully relocate 9770 earthquakes in the study area (shown in Figure 2) with errors of ∼40 m horizontally and ∼120 m vertically, estimated from bootstrap test removing one station at a time. Results of all processing steps are detailed in Appendix B. Aftershocks occur as shallow as ∼2 km depth, consistent with the refraction study of *Fuis and Kohler* [1984] showing that sedimentary units in the Salton Trough and surrounding region extend to depths between 3 and 4 km. Seismicity reaches maximum depths of ∼11 km, consistent with the suggested seismogenic depth to the northwest estimated from seismicity along the Elsinore Fault [*Magistrale and Rockwell*, 1996]. Hypocentral locations and origin times are given in the supporting information.

[16] Seismicity resulting from the final relocation step is no longer cloud-like and shows planar structures. In map view, linear bands of seismicity trend toward the northwest, with conjugate bands striking toward the northeast (Figure 2). We compare the relocated seismicity with triggered surface slip mapped by *Rymer et al.* [2011] and find clear agreement between the seismicity and mapped northeast trending faults in the Yuha Well Fault Zone and the Yuha Fault. Additionally, aftershocks align along the eastern branch of the northwest trending LS-E fault. Several smaller northwest and northeast trending lineations are also discernable in the seismicity, which do not appear to be associated with faults mapped by *Rymer et al.* [2011], particularly the NE trending band of seismicity to the NW of the Yuha Fault and smaller NW trending bands toward the east and parallel to the LS-E. In three-dimensional cross sections, relocated seismicity forms distinct planar features. For example, en echelon faulting of the Yuha Well Fault Zone persists at depth on individual fault planes with approximately vertical dips (Figure 3). The seismicity highlights planes that are small (< ∼5 km) in both the along-strike and along-dip directions. In many cases (e.g., LS-E and along the Yuha Well Fault Zone) the plane highlighted by the seismicity, projected to the surface, correlates well with mapped faults. Additionally, the seismicity adjacent to the LS-E appears to be steeply dipping toward the NE (Figure 3) and separated from nearby events, suggesting that it is not connected to neighboring faults at depth.

6. Discussion

[17] We relocate over 9500 aftershocks that occurred in the Yuha Desert following the EMC earthquake during a

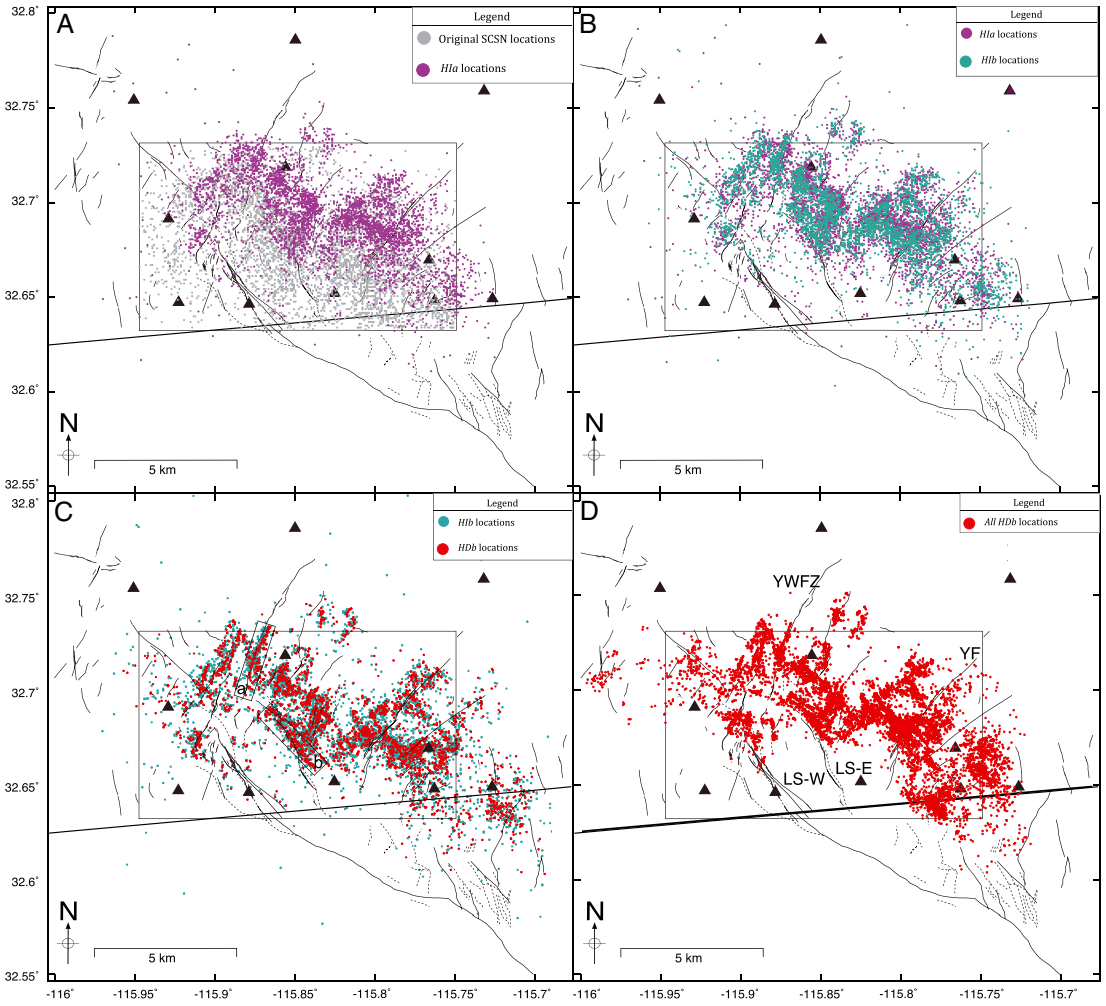

Figure 2. Relocation results from the data-processing scheme outlined in Figure A1. Results of the relocation procedure for events with manually detected phase arrivals and the relocation results of all events computed with manual and automatically detected phase arrivals. (a) Comparison of the original SCSN catalog locations (grey circles) and the first round of absolute relocations computed with Hypoinverse, labeled the *HIa* locations shown by the purple circles. Horizontal and vertical absolute location errors were reduced to 1.5 km and 2.3 km, respectively. RMS timing errors are reduced to 0.25 s. (b) *HIa* compared to *HIb* (green circles) locations computed with Hypoinverse with improved velocity model and station corrections that result from the Velest joint inversion. (c) *HIb* locations compared to the final *HDb* (red circles) locations computed with hypoDD. Relative location errors were estimated to be ∼20 m horizontally and ∼80 m vertically through a bootstrap analysis. The RMS timing errors were reduced to 0.004 s. Boxes a and b surround the seismicity shown in cross section in Figure 3. (d) Locations of all >9700 events relocated in this study. Faults mapped in the study area were observed to have triggered surface slip following the EMC earthquake [*Rymer et al.*, 2011]. Legend descriptions refer to phase of relocation process; refer to the appendix for details. LS-E: Laguna Salada-East branch, LS-F: Laguna Salada-West branch, YWFZ: Yuha Well Fault Zone, YF: Yuha Fault.

2 month deployment of eight temporary seismic stations. We use >110,000 manually identified *P* and *S* wave phase arrivals and >330,000 automatically detected arrivals to calculated absolute locations and invert for the best fitting 1-D velocity model with Hypoinverse and Velest, respectively. Precise relative locations are determined by inputting the 1-D velocity model, differential traveltimes, and cross-correlation delay times into hypoDD. The resulting earthquake locations allow us to investigate fault structure and strain accommodation in the fault step over region between the Elsinore and Laguna Salada faults as well as spatiotemporal migration of aftershocks and aftershock production rates, as described below.

6.1. A Complex Network of Conjugate Faults

[18] Combining the results of geologic field mapping with precisely located earthquakes enables the joint investigation of the three-dimensional fault structure. A variety of

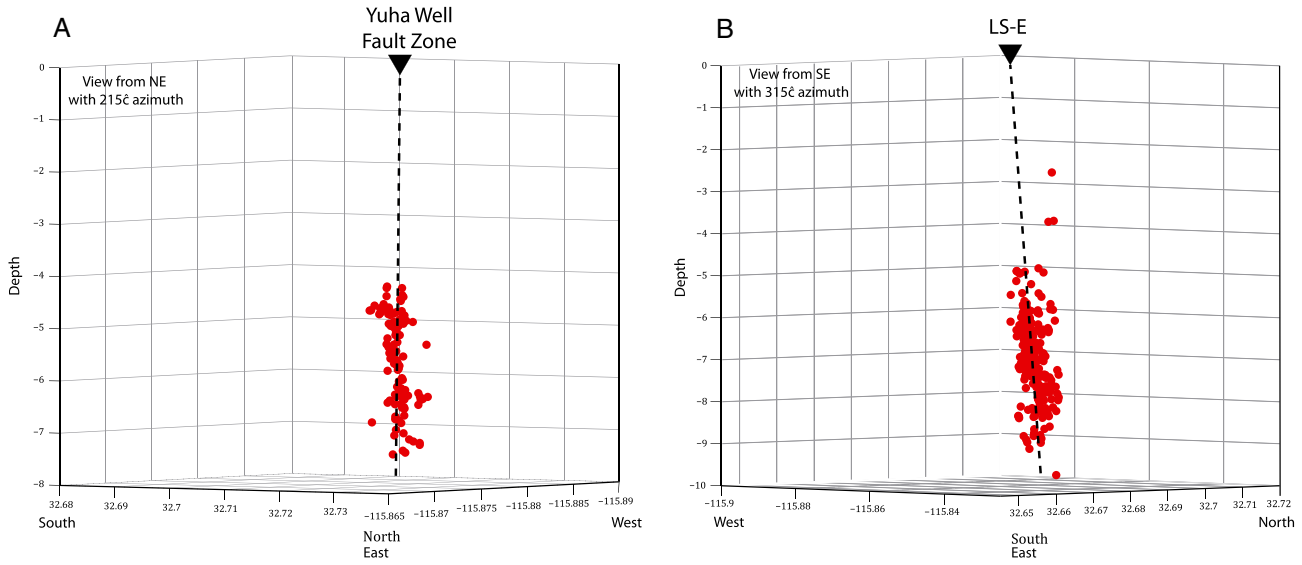

Figure 3. Three-dimensional cross-sectional views where seismicity (within 500 m of the surface trace) is highly correlated with mapped faults showing triggered surface slip. (a) A prominent fault of the Yuha Well Fault Zone is correlated with relocated seismicity (red circles) that forms a nearly vertical plane (heavy dashed line). The inferred plane dips ∼ 89°SE and projects to the surface (shown by inverted black triangles in Figure 2) at the approximate location of the fault mapped by *Rymer et al.* [2011]. (b) Seismicity highlighting the Laguna Salada-East branch (LS-E) (red circles) correlates well with the projection of the fault to the surface (heavy dashed line). The inferred subsurface extension of the LS-E dips ∼ 85°NE.

fault geometries, including flower structures (e.g., where complex surface faults coalesce onto simpler structures at depth) and conjugate faulting (e.g., where complex surface faults remain individual planes at depth) have been previously identified along major strike-slip faults. *Weldon II et al.* [2002] and *Harding* [1985, 1988] observe active flower structures along the San Andreas fault and other prominent strike-slip faults in Southern California, while *Sharp* [1967], *Nicholson et al.* [1986], and *Hauksson et al.* [2002] suggest that conjugate faulting is common in immature fault systems. Here multiple planar faults that extend the full depth of the seismogenic zone are apparent in three-dimensional visualizations of the relocated seismicity. A visualization of the fault structures is provided as supporting information to this paper. Evident planar features such as those of the Yuha Well Fault Zone show en echelon behavior at depth, mirroring the faults mapped at the surface. The seismicity adjacent to the LS-E forms a steeply dipping, planar feature that is separated from neighboring earthquakes. Figure 3 shows cross sections of the Yuha Well Fault Zone and the LS-E; the fault planes, inferred from the seismicity, project to the Earth's surface in approximately the same locations as the faults mapped by *Rymer et al.* [2011] as shown in Figure 2. Based on the relocated aftershocks, there is no indication of a larger, throughgoing fault that would be suggestive of a flower structure. Here faults extend to depth as individual, conjugate fault strands where northwest striking faults slip right-laterally, while the conjugate, northeast striking faults undergo left-lateral motion. The complex, unconnected fault structure in this small region is consistent with a complex set of conjugate faults along an immature fault system, similar to that shown by *Hauksson et al.* [2002] in the relocated aftershocks of the Hector Mine earthquake. A 3-D animation of the relocated seismicity in the Yuha Desert is provided as supporting information to this work.

[19] We also compare the final locations to previously mapped faults that experienced triggered surface slip coincident with the EMC main shock [*Rymer et al.*, 2011] (Figure 2). Surface mapping by *Rymer et al.* [2011] indicate that faults in the Yuha Desert display a variety of kinematic behavior, including conjugate right and left-lateral slip, as well as normal offsets. The Yuha Fault (unmapped prior to the EMC) is a northeast striking fault located between stations PNTO and MLDN toward the southeast of the study area that experienced nearly 50 mm of left-lateral triggered surface slip, and the en echelon left-lateral faults of the Yuha Well Fault Zone in the northwest of the study area experienced up to 19 mm of triggered surface slip [*Rymer et al.*, 2011]. The northwest striking LS-E and LS-W branches both experienced ∼40 mm of right-lateral triggered surface slip in addition to a small normal component of ∼2 mm on each fault. Interestingly, the LS-E branch shows eastside up extensional motion, while the LS-W shows westside up motion, creating a down-dropped graben between the segments. *Rymer et al.* [2011] note that they only map faults that exhibited obvious, recent surface slip related to the EMC earthquake, although several other fault strands were noted, but not recorded, during their field surveys. Slip observed by *Rymer et al.* [2011] is consistent with focal mechanism solutions computed by *Yang et al.* [2012] for northwest and northeast trending faults. We note a clear correlation between the mapped fault structure [*Rymer et al.*, 2011] and the relocated seismicity reported here. Relocated seismicity highlights both the mapped northwest trending right-lateral faults and northeast trending left-lateral faults. Earthquakes cluster along a northwest oriented lineation

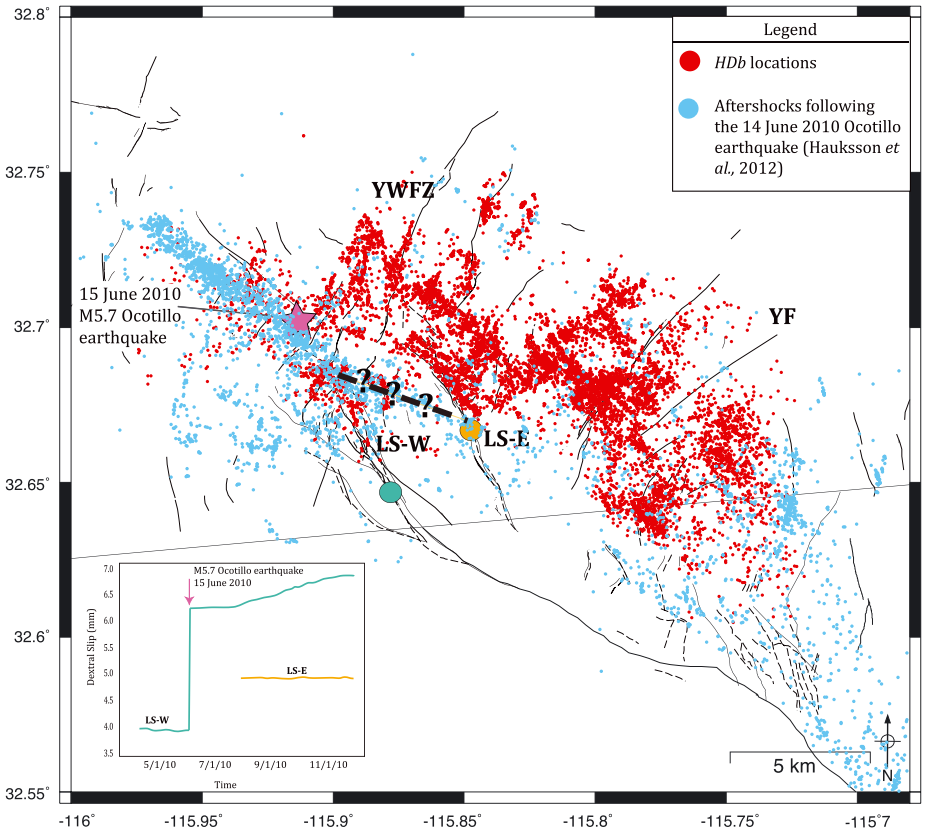

Figure 4. Comparison between the mapped triggered surface slip [*Rymer et al.*, 2011], relocated seismicity, and data collected from two creepmeters installed along the Laguna Salada-West and East branches (LS-W and LS-E). Red circles indicate the seismicity relocated in this work, while blue circles are seismicity relocated by *Hauksson et al.* [2012] following the 15 June 2010 *M* 5.7 Ocotillo earthquake (hypocenter shown by the pink star). The green and yellow circles along the LS-W and LS-E branches, respectively, represent the two creepmeters installed on 10 April and 14 August 2010, respectively. (inset) Creepmeter time series (Bilham, personal communication, 2012) show ∼2 mm of surface creep on the LS-W occurring coincident with the Ocotillo earthquake. While the LS-E creepmeter was not installed during this event, surface displacement was not observed in the precise caliper measurements taken along this fault segment. Bold dashed line illustrates possible connecting fault between the LS-W and LS-E illuminated in seismicity following the Ocotillo earthquake. YWFZ; Yuha Well Fault Zone, YF; Yuha Fault.

(LS-E segment) as well as several smaller northeast trending lineations ∼2.5 km east of the LS-E; these prominent features align with the mapped faults that exhibited the greatest amount of surface slip [*Rymer et al.*, 2011]. There are also smaller northwest and northeast trending lineations throughout the study area that do not appear to be associated with faults mapped by *Rymer et al.* [2011]. This suggests that slip in the Yuha Desert is accommodated both by faults that slip only at depth and by faults that slip both at depth and at the surface, at least during this particular event.

[20] It has been shown, both observationally [*Antolik et al.*, 2004; *Wesnousky*, 2006; *Fletcher et al.*, 2010] and in dynamic models [*Duan and Oglesby*, 2006; *Lozos et al.*, 2011; *Harris and Day*, 1993, 1999], that large earthquakes can rupture multiple fault segments, negotiate geometric complexities, and jump large fault step overs. *Fletcher et al.* [2010] showed that the EMC main shock rupture jumped an ∼11 km extensional step over. The ability for rupture to jump a fault step over is limited by several factors including step over width, transpressional versus transtensional settings, and the presence of a linking segment [*Duan and Oglesby*, 2006; *Lozos et al.*, 2011]. Rupture propagation is likely further complicated by the addition of complex faulting within the step over region. In the case of the EMC earthquake, rupture ceased ∼4 km southeast of the Yuha Desert (the step over region between the Elsinore and Laguna Salada faults) where an intricate patchwork of conjugate faults is seen. It is possible that the EMC rupture might have ended in the area because there was no single fault strand large enough to support the continuation of the rupture. We suggest that the fault pattern in the Yuha Desert may have acted as a barrier to rupture, inhibiting the EMC earthquake from jumping onto larger fault traces to the north and driving strain to be accommodated along smaller, adjacent fault segments.

[21] Several faults in Southern California that compose the plate boundary system north of the EMC main shock rupture, such as the Superstition Hills, Elmore Ranch, and

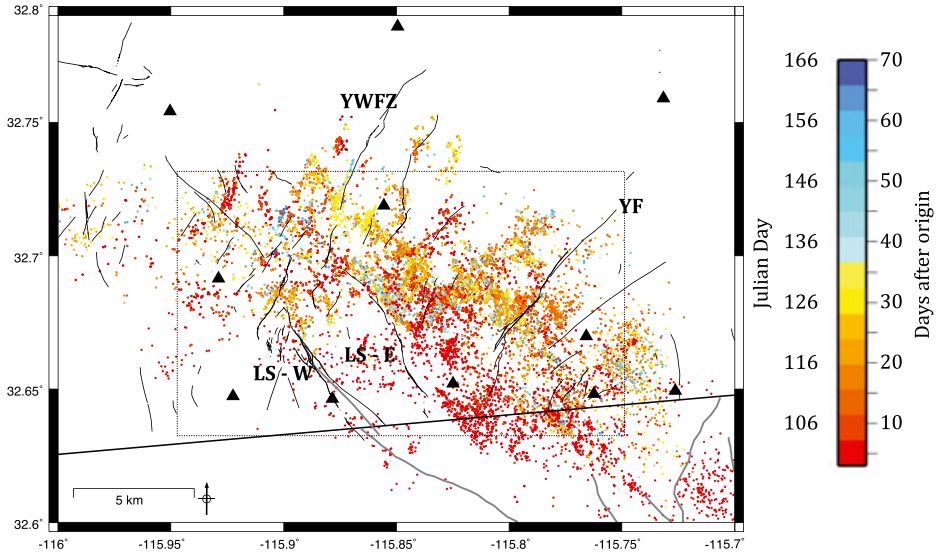

Figure 5. Relocated seismicity plotted as a function of time after the EMC main shock. A nonuniform expansion of aftershock activity is seen following the main shock. To further investigate the spatial and temporal behavior of the aftershock distribution, we subdivide the data set into equal-sized subsets based on number of events in Figure 6. LS-F, Laguna Salada-West branch; LS-E, Laguna Salada-East branch; YWFZ, Yuha Well Fault Zone; YF, Yuha Fault.

Imperial faults, have been shown to creep [e.g., *Goultry et al.*, 1978; *Bilham*, 1989; *Hudnut and Sieh*, 1989; *McGill et al.*, 1989; *Lyons et al.*, 2002]. Two creepmeters were installed along the LS-W (10 April 2010) and LS-E (August 2010) faults following the EMC main shock to investigate the slip behavior of these two fault segments [*Rymer et al.*, 2011]. Figure 4 shows the seismicity, mapped faults, and creep time series (Bilham, personal communication, 2012). Neither fault experienced observable creep following the EMC earthquake; however, ∼2 mm of triggered creep along the LS-W segment occurred coincident with the 15 June 2010 M 5.7 Ocotillo earthquake (Figure 4). Caliper measurements (10 μm precision) made along the LS-E on 12 May 2010 and again before the installation of the creepmeter in August 2010 show no surface offset [*Rymer et al.*, 2011]. When we examine the relocated seismicity, we find that the LS-W branch, which was not seismically active following the EMC main shock, experienced a large number of events following the Ocotillo earthquake (Figure 4). In contrast, the LS-E was very seismically active in the 2 month period following the EMC event, but seismicity from *Hauksson et al.* [2012] shows very little activity along this segment following the Ocotillo earthquake. These observations suggest that seismicity rates and slip behavior are spatially and temporally variable in the Yuha Desert and are likely influenced by local static stress changes, which is the focus of future work.

6.2. Spatiotemporal Aftershock Behavior

[22] The spatiotemporal distribution of aftershock sequences can provide information about stress changes induced by a large main shock [*Toda and Matsumura*, 2006], aftershock rates and migration patterns [*Dieterich*, 1994; *Helmstetter et al.*, 2003], postseismic deformation and/or afterslip [*Peng and Zhao*, 2009], fluid migration [*Noir et al.*, 1997], and other phenomena. Several studies show increased aftershock activity adjacent to areas of high slip and high moment release [e.g., *Wald et al.*, 1995; *Thio and Kanamori*, 1996; *Ma and Chan*, 2005]. Others show higher aftershock rates in areas with increased shear and Coulomb stress near the ends of a fault rupture [e.g., *Mendoza and Hartzell*, 1988; *Toda et al.*, 2005]. *Freed* [2005], *Ratchkovski et al.* [2003], and *Robinson et al.* [2006] show that zones of increased stress are spatially heterogeneous along faults with complex geometries or step overs, with higher aftershock activity in step over and branching regions. Studies of aftershock sequences also often show a migration of activity away from the main shock epicenter through time [e.g., *Tajima and Kanamori*, 1985; *Peng and Zhao*, 2009].

[23] Figure 5 shows the relocated aftershocks color coded by time after the EMC main shock suggesting there is not a clear expansion or migration of the aftershock locations away from the main shock epicenter (e.g., from southeast to northwest). However, we do note some interesting spatiotemporal behavior of aftershocks. To further investigate, we divide the aftershocks into equal-sized data subsets by total number of events with ∼2400 events in each subplot of Figure 6, so that the first 2442 aftershocks to occur are shown in Figure 5a, the subsequent 2442 aftershocks are shown in Figure 5b, etc. Generally, we observe that aftershocks are dispersed throughout the relatively small region during each of the four time periods. However, rather than events occurring on the same fault section throughout the study period, seismicity seems to jump between adjacent fault strands. Below we briefly describe the migration of seismicity during the four time periods shown in Figure 6.

[24] Early in the aftershock sequence and in the northwestern portion of the study area (Figure 6a, area i) we observe short (<3 km), northeast trending fault segments in the seismicity. No seismicity is apparent along the LS-W (area ii), but some aligned seismicity occurs north of the mapped LS-E (area iii). The central portion of the study area

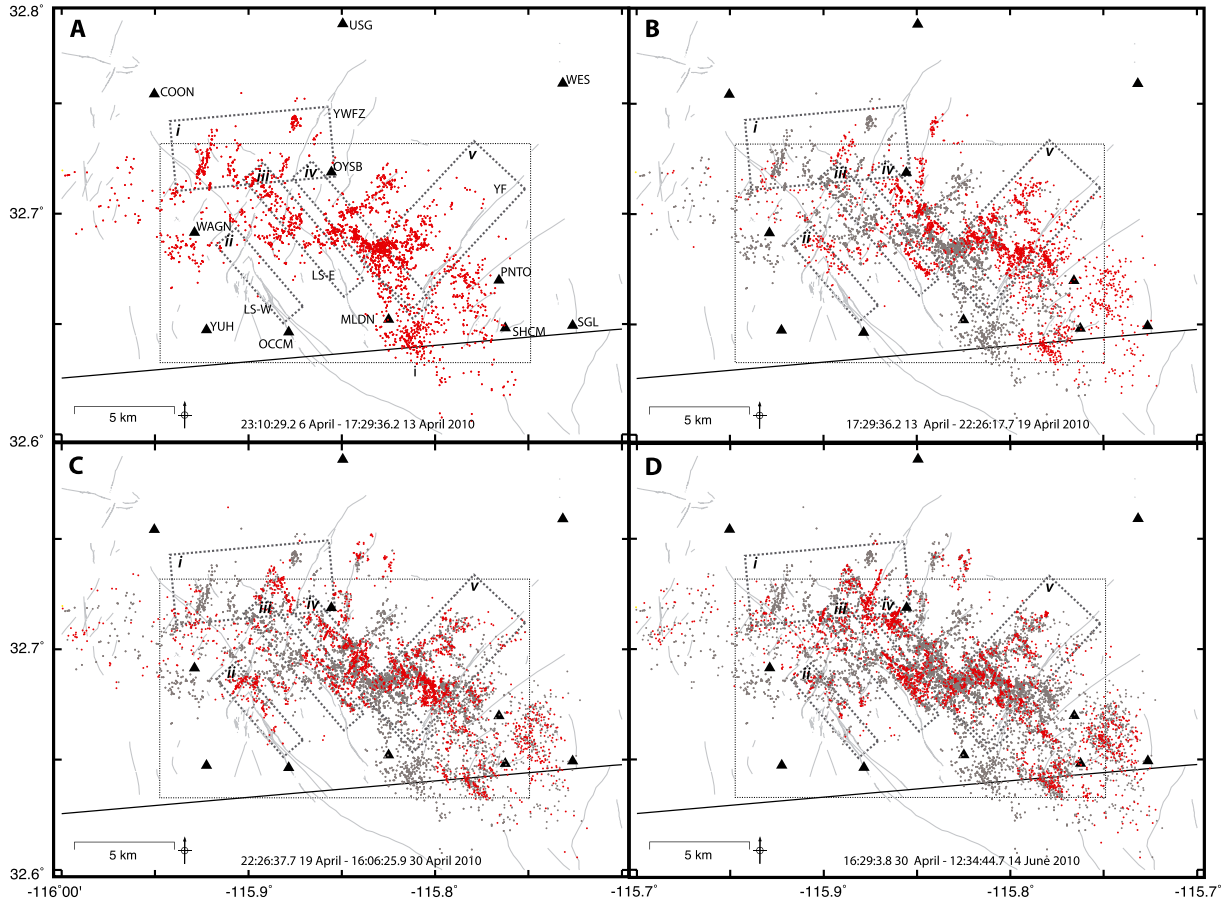

Figure 6. Relocated seismicity divided into (a–d) four subsets, each containing 2442 events. Each sequential subset contains the 2442 events in that period plotted in red, as well as events from all previous segments plotted in grey. The time period (HH:MM:SS.ms Day Month Year) is listed in each panel. Migration patterns are most easily observed in five areas (i–v). Examination reveals that small, individual fault strands are active individually for short time periods. Seismicity appears to migrate along and between adjacent fault segments with time. Interestingly, the Laguna Salada-East branch (LS-E) only becomes active ∼35 days following the EMC and remains active for the duration of the study (71 days following the EMC); however, there are relatively few earthquakes along the Laguna Salada-West branch (LS-W) during this same period. YWFZ, Yuha Well Fault Zone; YF, Yuha Fault.

shows seismicity aligned in both northeast and northwest trends, with a very active band of northwest trending seismicity located ∼2 km east of the LS-E (area iv). Both the north end and south end of this segment terminate into active northeast trending fault segments. The southeastern part of the study area appears to have more diffuse seismicity that is not readily resolved onto planes.

[25] The second period of seismicity, shown in Figure 6b, suggests most of the segments in the northern part of the study area have turned off, with a single new segment activated (area i). North of the end of the mapped LS-W (area ii), there is some diffuse seismicity where there were no previous events, but very little seismicity occurs near the LS-W itself. Seismicity appears along a small section of the mapped LS-E (area iii), and events on the previously active segment to the east (area iv) appear to migrate to the northwest. This period also reveals seismicity along a northwest trending mapped fault near station OYSB that was not active during the initial aftershock period. Farther south, the Yuha Fault (area v) is more apparent in the seismicity as well as several new diffuse regions of seismicity near the California-Mexico border to the southeast of the study area.

[26] During the third period of seismicity, aftershock distributions are fairly similar to the immediately preceding time period. However, in area i we see seismicity along the previously active, northeast trending segment merging with seismicity along what appears to be an extension of the northwest trending fault highlighted in area iv. In the final time period, we note that activity continues and perhaps even increases along the LS-E (area iii), but there is essentially no activity along the LS-W (area ii). And we observe that the southern end of the northeast trending Yuha Well Fault Zone becomes active for the first time.

[27] Examination of the relocated catalog indicates that the LS-E branch only becomes active after ∼35 days following the EMC earthquake and remains active for the duration of the study (71 days following the EMC earthquake). While it is outside the scope of this paper, it is worth mentioning that the LS-W branch remains essentially inactive until the *M* 5.7 Ocotillo earthquake on 15 June 2010, while most of

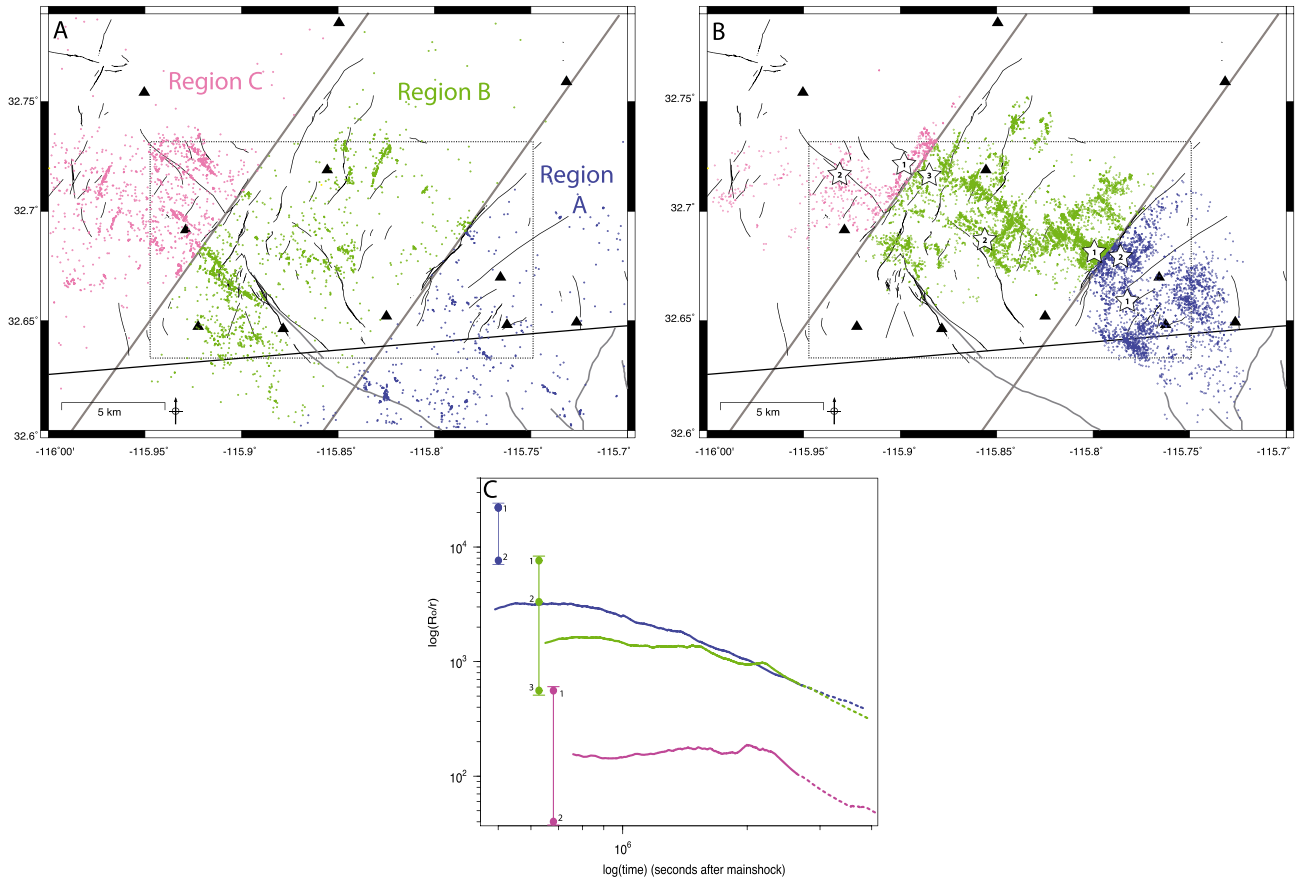

Figure 7. (a) Background seismicity [*Hauksson et al.*, 2012] subdivided into three regions by increasing distance from the main shock hypocenter. (b) Relocated aftershocks following the EMC main shock, also subdivided by increasing distance from the main shock hypocenter. (c) Earthquake production rate following the EMC. Each curve is color coordinated to one of the three regions. The peak aftershock rates are roughly consistent with the rate-and-state law for earthquake production following a stress step shown in equation (1). The dotted portions of the curves represent the time period following the removal of three temporary stations. Bars represent the plausible range of predicted earthquake rates for a given area of each region (denoted by numbered labels that correspond to the numbered stars in Figure 7b) assuming the calculated Coulomb stress change values and normal stress equal to 55 MPa.

the eastern Yuha Desert shows productive seismic activity. Following the Ocotillo earthquake, activity reverses and the eastern Yuha Desert shows little seismicity, while the majority of the seismicity is aligned along the LS-W branch. This behavior continues at least until 30 June 2011, the last day of seismicity relocated by *Hauksson et al.* [2012].

6.3. Aftershock Production Rates

[28] To quantify the effects of the stress change induced by the EMC main shock on the rate of earthquake production in the Yuha Desert, we employ the constitutive relationship described in *Dieterich* [1994]. The instantaneous seismicity rate following a stress step can be derived as follows:

$$\frac{R_o}{r} = \exp\left(\frac{\Delta S}{a\sigma}\right) \tag{1}$$

where r and R_o are the seismicity rates before and after the stress step, respectively, ΔS is the Coulomb stress change, a is the constitutive parameter with laboratory values ranging from 0.005 to 0.015, and σ is the normal stress. The nominal minimum and maximum magnitudes are ~1.4 and ~4.8, respectively. Assuming a uniform station coverage, the range of magnitudes remains the same and rates are calculated based on all the locatable events. In this study, three of eight UC-RAMP stations were removed on 15 May 2010; therefore, the aftershock production rate may be underestimated after this point (marked by the dotted line segments in Figure 7). The consistent slope of the decay suggest the range of magnitudes presented before and after 15 May 2010 are likely similar. To estimate ΔS for each region, we compute the static Coulomb stress change due to the EMC main shock using the Coulomb 3.3 software [*Toda et al.*, 2011]. We use a uniform slip model with an average of 2.5 m of slip, along a 120 km long, vertically dipping, right-lateral fault striking 312° [*Wei et al.*, 2011]. Coulomb stress change was computed along vertical receiver faults striking 35°, with a rake of 180°. No significant differences in the computed Coulomb stress change were noted if we instead chose conjugate receiver faults striking ~ 320°.

[29] To determine whether the seismicity generally follows the relationships described by *Dieterich* [1994], we

divide the study area into three regions that cover approximately equal areas (A, B, and C in Figure 7) to compare the rate of earthquake production across the region that result from stress changes due to the EMC main shock. This method provides an approximate seismicity rate based only on the selection of constitutive parameters, and it does not require knowledge of fault orientation. The computed Coulomb stress change is 5.0 bars, 4 bars, and 2.5 bars, in regions A, B, and C, respectively. Assuming these Coulomb stress changes and setting $a = 0.01$, values of normal stress are calculated to be 62.5 MPa, 54.7 MPa, and 50 MPa for each of the regions, respectively. Taking the average value of normal stress (based on the assumption that this value should not change over a small area), we compute the current rate of seismicity over the background rate that would be expected in each region. The "current" seismicity is taken to be those events that occurred during the deployment of the UC-RAMP stations (i.e., 6 April through 14 June 2010), while the background seismicity is defined as all events occurring in the same regions in the 30 year period preceding the EMC main shock.

[30] We find that in region A, seismicity rates increase by a factor of 3000 over the background rate, while farther from the main shock rupture, seismicity rates increase by a factor of 100, a more moderate increase over the background rate, as expected due to the smaller stress increase (Figure 7). If we compare the earthquake rates predicted from the calculated Coulomb stress, we note that there is relatively good agreement for regions B and C with an underprediction of events in region A (see Figure 7). While we use typical values of a and σ, the lower observed earthquake production rate in region A might suggest that lower values for these parameters should be used. However, we do not have any independent information to better constrain a and σ. Overall, the shape of the earthquake production curves plotted in Figure 7 are roughly consistent with the theoretical rate curves derived by *Dieterich* [1994]. At some time after the stress step the curves are expected to converge, as seen for the curves representing regions A and B. However, the rate curve for region C does not converge with curves A and B due to a higher background seismicity rate in region C. The higher background seismicity rate likely reflects the higher strain rates to the north near the Elsinore Fault which are on average 3 times higher than for the Laguna Salada fault to the south.

7. Conclusions

[31] In summary, we detect and relocate ~9700 aftershocks in the Yuha Desert region during a 2 month temporary deployment of seismic stations following the 4 April 2010 M_w 7.2 El Mayor-Cucapah earthquake. We find that the relocated seismicity falls along right-lateral northwest and left-lateral northeast trending conjugate fault structures within the Yuha Desert and correlates well with the mapped faults that exhibit triggered surface slip as mapped by *Rymer et al.* [2011]. Depths of the events are between 2 and 11 km, consistent with previous studies of the southern Elsinore Fault [e.g., *Magistrale and Rockwell*, 1996]. The aftershock locations suggest that fault segments remain as distinct, individual structures at depth, revealing a complex patchwork of conjugate faults. Conjugate faulting is supported by the orientation of faulting (i.e., strike of NW and NE trending fault structures separated by ~ 35° to 60°) and the sense of displacement along the fault segments (i.e., left-lateral motion on the northeast trending Yuha Fault and Yuha Well Fault Zone and right-lateral/normal motion on the northwest trending LS-W and LS-E [*Rymer et al.*, 2011]). The complex fault structure, minimal fault-induced topographic expression, and variable slip direction (i.e., right- and left-lateral slip) are indicative of a fault system that has not accommodated much total strain. This is additionally supported by the low slip rates on the southern Elsinore (up to 6 mm/yr) [*Magistrale and Rockwell*, 1996] and northern Laguna Salada (~2 mm/yr) [*Mueller and Rockwell*, 1995] faults.

[32] We do not observe a clear migration of the relocated aftershock hypocenters with time away from the EMC main shock epicenter. Closer examination reveals that seismic activity temporally clusters onto small, linear features. In some instances, the features highlighted by seismicity align with fault segments previously mapped by *Rymer et al.* [2011]. Seismicity appears to migrate with time along and between these linear features. The complexity of the spatiotemporal migration may be due to the restricted study area and deployment period.

[33] The main trace of the Laguna Salada fault, which last ruptured in the M 7.2 1892 earthquake, splits into the LS-W and LS-E branches ~5 km south of the Yuha Desert. The parallel NW trending branches experience a component of right-lateral and normal displacement and are separated by a maximum of ~4 km at the surface [*Isaac*, 1987; *Rymer et al.*, 2011]. Both faults are reported to dip at the surface between 75° and 90° to the west [*Isaac*, 1987]. Seismicity suggests that the main strands of the LS-W and LS-E are dipping subvertically away from each other and, therefore, may not merge onto a throughgoing fault at depth. Seismicity on the LS-E occurs only during the period between the EMC and Ocotillo earthquakes (~9 May and 14 June 2010) at depths between 3 and 11 km and appears to be constrained on a vertical to subvertical east dipping plane. Seismicity only occurs along the LS-W following the Ocotillo aftershock, at depths between 2 and 11 km, on approximately vertical to subvertical west dipping plane. It is interesting to note that the seismicity following the Ocotillo event suggests that there is a subvertical, northwest striking segment that may link the LS-W and LS-E (black dashed line in Figure 4).

[34] In conclusion, relocated seismicity suggests that the conjugate northwest and northeast pattern of faulting seen at the surface in the Yuha Desert extends throughout the seismogenic zone. Within this limited area, we see very complicated spatiotemporal behavior in aftershock occurrence. On a broad scale, aftershock activity in the eastern Yuha Desert is vigorous following the EMC main shock but appears to shut off following the Ocotillo event. Detailed examination of the seismicity shows that individual fault segments are active for a very limited period, perhaps suggesting main shock/aftershock processes at a very limited spatial scale. To more fully understand the complex nature of faulting in the region, future work will include Coulomb stress transfer modeling, rupture propagation modeling through step over regions with complex fault structures, and 3-D spatiotemporal analysis of the seismicity.

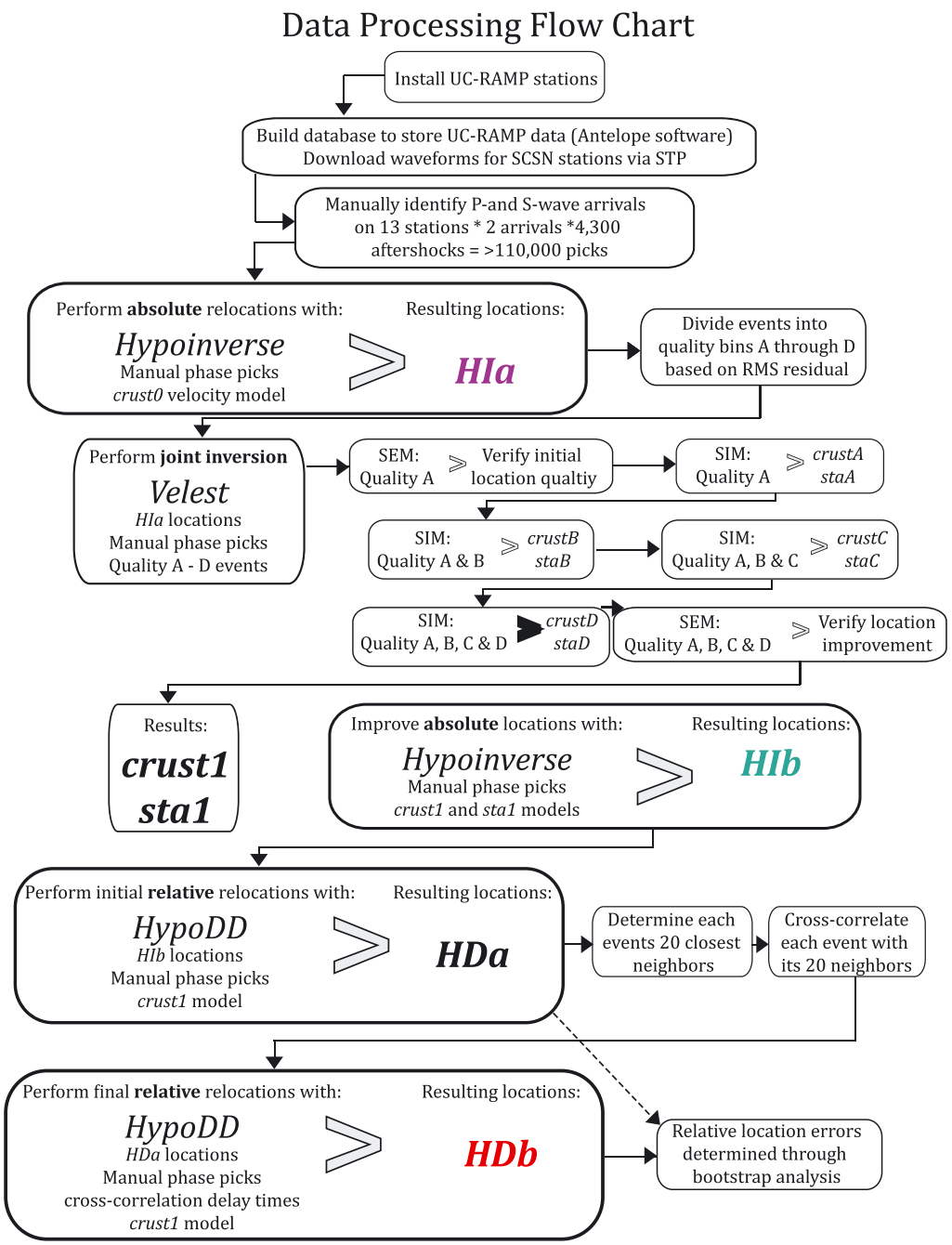

Figure A1. Flow chart of the data processing scheme that was used in this analysis. The resulting location codes (i.e., *HIa*, *HIb*, *HDa*, and *HDb*) are color coded according to the color of their corresponding locations as shown in Figures 2a–2c: *HIa*, *HIb*, and *HDb*.

Appendix A: Detailed Relocation Procedure

[35] We undertake a multistep approach to compute high precision earthquake locations. This procedure uses three algorithms: Hypoinverse [*Klein*, 2002], Velest [*Kissling et al.*, 1994], and hypoDD [*Waldhauser and Ellsworth*, 2000]. The steps of our method are outlined in the flow chart in Figure A1.

A1. Manual Phase Picking of SCSN Catalog Events

[36] To improve the initial locations of the ~4323 events in the SCSN catalog, we manually identify *P* and *S* wave arrivals on the vertical (*Z*) and horizontal (N/E) components of all 13 stations (5 SCSN and 8 UC-RAMP), respectively. Waveforms from the SCSN stations are obtained via the Seismogram Transfer Program (STP) from the Southern California Earthquake Data Center. One-minute waveform records are extracted from the SCSN archive starting at the event origin time from the SCSN catalog. For consistency, all *S* waves are picked at the first arriving *S* energy on either component but are marked on the north component. Before processing, we remove the mean and band-pass filter the waveforms between 1 and 15 Hz. In general, the accuracy of manually identified phase arrivals is greater than that of

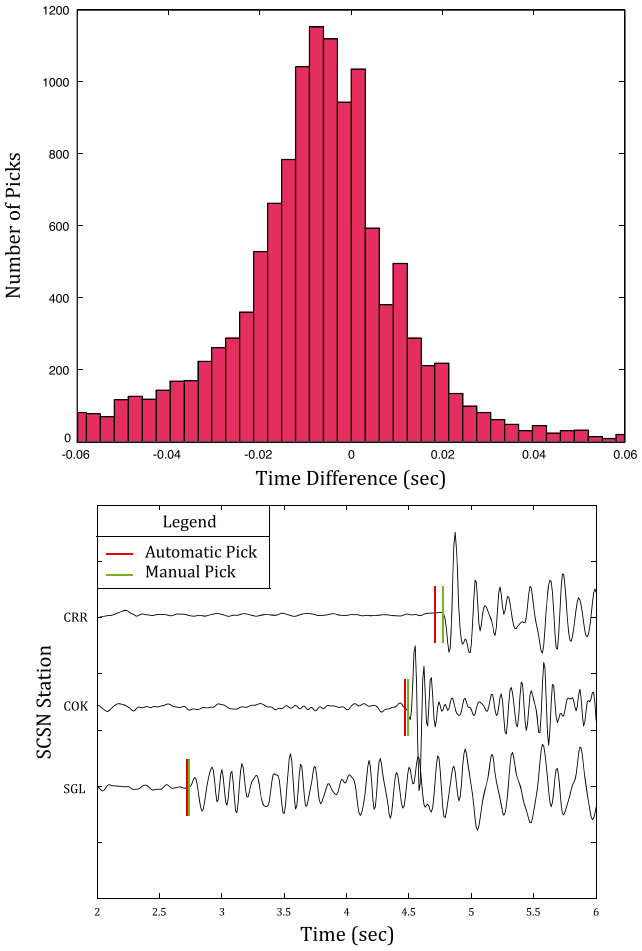

Figure A2. (top) Histogram of time offsets between manual and automatic phase arrival picks. Negative values represent waveforms for which an automatic pick was made before a manual pick. The automatic and manual pick offsets range from 0 to 3.0 s, with most picks within 0.06 s. (bottom) Diagram showing the difference in automatic (red line) versus manual (green line) *P* wave picks for a *M* 2.72 earthquake on 23 April 2010 recorded by three of the five SCSN stations used in this study.

an automatic pick. Figure A2 (top) shows a histogram of the timing offset between automatic and manually identified picks, and Figure A2 (bottom) shows an example waveform comparing the automatic and manual picks. We find the difference between automatic and manual picks ranges between 0 and ∼3.0 s, with most picks within 0.06 s.

A2. Detection of Additional Aftershocks

[37] Many small aftershocks in the Yuha Desert are not reported by the SCSN due to poor azimuthal station coverage, increased event-station distance, and small event separation times. Therefore, we examine the continuous waveform data recorded by the UC-RAMP stations to supplement the SCSN catalog. Waveform data from the UC-RAMP stations are processed and examined using the Antelope v. 5.1-64 software distributed by Boulder Real Time Technologies (BRTT). We use the Antelope short-term/long-term average (STA/LTA) algorithm *dbdetect* to automatically detect arrivals. The ability of a STA/LTA algorithm to accurately detect arrivals is primarily dependent upon the choice of window and signal-to-noise ratio (SNR) threshold. These parameters must be adjusted through trial and error as they vary depending on whether regional or local event detections are desired. To detect local events in our data set, we set the short-term average window to 0.1 s, the long-term average window to 1.5 s, and the SNR ratio to 5. *dbdetect* generates a list of absolute detection times, but detections are not assigned a phase type or associated with an earthquake.

[38] For phase types (e.g., *P* or *S*) to be identified and events to be declared, detected arrivals on a minimum number of stations within a specified time window are associated. The process of event association is completed using the Antelope program *dbgrassoc*. *dbgrassoc* undertakes a least-squares grid search on a user-defined 3-D grid of potential hypocenter locations to reduce the traveltime residual between the theoretical arrival times and automated detections from *dbdetect*. Theoretical traveltimes are computed using the Antelope program *ttgrid* with the *tauP* method assuming the IASP91 velocity model for a ∼50 by ∼50 km grid centered on 32.77°N, –115.85°E. We use horizontal and vertical grid spacing of ∼1 km. The association detected over 39,000 earthquakes, 17,000 of which are located within the study area. Of these events, ∼2500 are also listed in the SCSN catalog.

A3. Absolute Locations Using Hypoinverse

[39] The Hypoinverse algorithm [*Klein*, 2002] locates the events using both the manual and automatic phase arrivals. We use a modified 12-layer 1-D starting velocity model (*crust*0) from the SCEC Community Velocity Model-version 4 for the Imperial Valley region (Figure A3) and a V_p/V_s ratio of 1.68, estimated for the Yuha Desert using Wadati diagrams of 100 events [*Juliá et al.*, 2009; *Frassetto et al.*, 2011]. The starting or "trial" location of each event is placed 7 km below the station with the earliest arrival. Hypocenters are allowed to move freely away from the trial location, within the constraints of the damping parameters. The damping parameters used in this study are as follows: 10, 15, 0.1, 0.9, 0.0275, 0.020, 0.6, 50, and 50 for DXFIX, DZMAX, DZAIR, DAMP, EIGTOL, RBACK, BACFAC, DXMAX, and D2FAR, respectively. For a detailed explanation of these parameters, please see *Klein* [2002]. The parameters depend on the spatial extent of the seismicity, depth of the seismogenic zone, and station distribution and are determined by trial and error. The initial location is adjusted through a least-squares iterative approach until the minimum residual between the observed and predicted traveltimes is reached. Predicted traveltimes are determined by 3-D ray tracing using the velocity model described above. In this first round of iterations, the *P* wave and *S* wave picks are weighted 100% and 75%, respectively. The *S* wave picks are down-weighted because they are generally less accurate than *P* wave picks and can be obscured by *P* wave coda.

[40] To estimate the hypocentral error, Hypoinverse computes the variance matrix, which is derived from the matrix containing the partial derivatives of the traveltime with

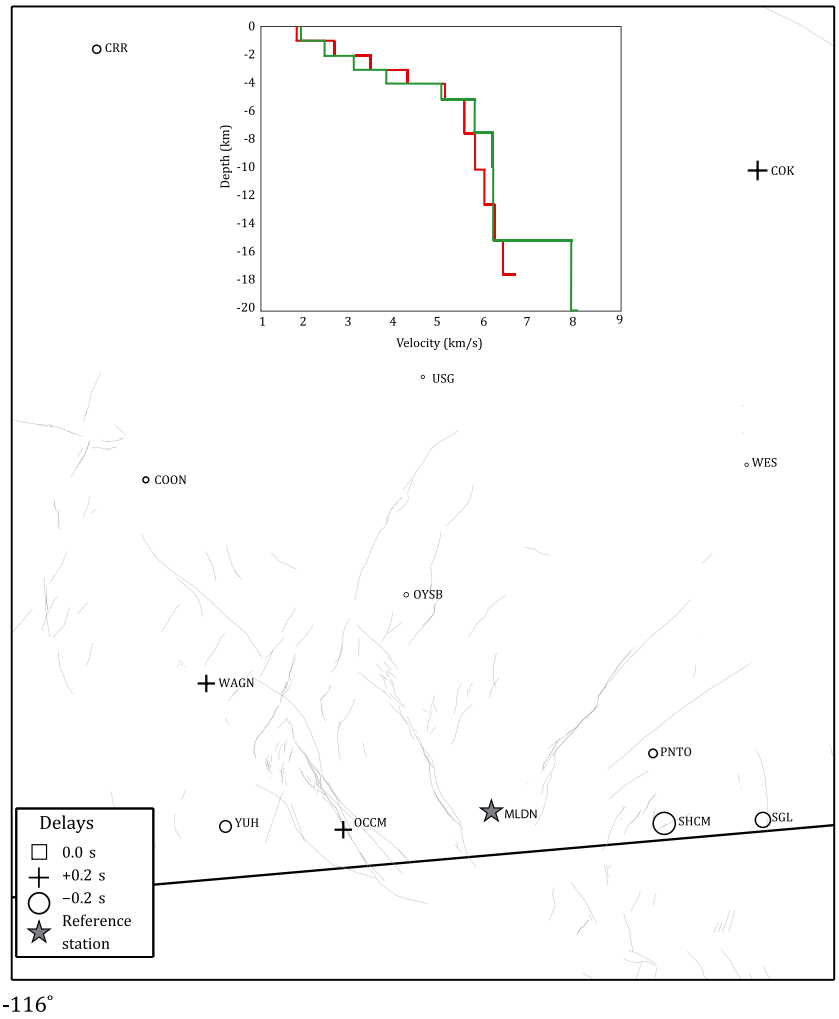

Figure A3. Map of best fitting station corrections and resulting velocity model (inset diagram, green) from the Velest joint inversion. The a priori (*crust*0) velocity model (inset diagram, red) was modified from the SCEC Community Velocity Model, version 4 (CVM-v4) for the Imperial Valley region and used in the initial absolute location determination with Hypoinverse.

respect to changes in the hypocenter location. The 4 × 4 covariance matrix containing the hypocentral parameters (x, y, and z) plus the origin time (t) is subdivided into the 3 × 3 submatrix containing only the spatial coordinates and rotated into the principal component coordinate system of the hypocentral solution. Standard errors are calculated by taking the square roots of the eigenvalues of the 3×3 covariance submatrix. These standard errors correspond to the 32% confidence ellipsoid interval (i.e., the true hypocenter has a 32% likelihood of lying within the ellipsoid defined by the eigenvalues and eigenvectors of the covariance matrix). The 32% confidence ellipsoid is the 2σ error ellipsoid in three dimensions. The standard errors should be multiplied by a factor of 2.4 to achieve the 95% confidence ellipsoid. Additionally, to correctly account for systematic (i.e., velocity structure) and random (i.e., picking) errors, the covariance matrix can be weighted with the ERCOF (the coefficient of the RMS traveltime residual) and ERR (e.g., assumed reading and timing error) parameters within Hypoinverse, respectively, prior to the inversion process [*Klein*, 2002]. For cases where the velocity model is known with confidence (i.e., estimated through a joint-inversion process) and where picking errors are reduced by manual picking, these parameters can be down-weighted significantly. In our analysis, these parameters were given full weight; therefore, the likelihood of the true hypocenter lying with the error ellipsoid defined by the covariance matrix is likely greater than 32%. Hypoinverse reports vertical errors as the projection of the longest principal axis onto a vertical line running through the hypocenter and horizontal errors as the length of the longest principal axis, as viewed from above, and projected onto a horizontal plane [*Klein*, 2002].

A4. Improved 1-D Velocity Model and Station Correction Using Velest

[41] To improve the absolute locations determined using Hypoinverse, we employ the joint hypocenter inversion algorithm Velest [*Kissling et al.*, 1994]. Given an initial set of locations and phase arrivals, Velest jointly inverts for the best fitting earthquake locations, 1-D velocity model, and station corrections. Station corrections mitigate the

Table A1. Aftershocks Binned Based on the RMS Residual From Hypoinverse[a]

Quality Bin	Minimum RMS (s)	Maximum RMS (s)	Total Number of Events
A	0	0.12	420
B	0.13	0.17	1942
C	0.18	0.23	1536
D	0.24	1	157

[a]The joint inversion for the optimal 1-D velocity model and station corrections was performed with the Quality A earthquakes. Quality B through D event bins were used to test the stability of the best fitting velocity model and station corrections.

effect of near-surface velocity heterogeneities beneath a station without requiring a 3-D velocity model. Velest is a proven technique for 1-D velocity model determination with local and regional arrays [e.g., *Chaiarabba and Frepoli*, 1997; *Smith and Kasameyer*, 1997; *Ojeda and Havskov*, 2001; *Pontoise and Monfret*, 2004; *Waldhauser and Tolstoy*, 2011; *Sumy et al.*, 2013] and, thus, is the preferred method to use in the Yuha Desert.

[42] Here we use only events for which we have manually identified phase arrivals and subdivide our preliminary absolute locations (*HIa*) based on the RMS residual from Hypoinverse. We classify these events as "Quality A" events and further partition the remaining ∼3600 events into Quality B through D categories by RMS residual (Table A1).

[43] We initially relocate the 420 Quality A events in the single-event mode (SEM) of Velest. SEM inverts for new locations based on the a priori (*crust*0) velocity model. This step is used to verify that the locations are not significantly different from the *HIa* locations. The first joint inversion in simultaneous mode (SIM) uses the SEM locations of the Quality A events and outputs a modified velocity model (*crustA*), station corrections (*staA*), and refined hypocenters. Then, the Quality A events are run through SEM with *crustA* and *staA* to verify location improvement. We use default parameter values, except for the V_p/V_s ratio, which we measured specifically for the Yuha Desert as described above. As Velest was originally developed for local events, the default parameters are relevant here. A detailed explanation of all parameters is given in the Velest users manual [*Kissling et al.*, 1994].

[44] Quality B, C, and D events are then added sequentially to the Quality A events and jointly inverted; each inversion incorporates the improved event locations, velocity model, and station corrections from the previous step. Small perturbations to the input velocity model and station corrections are made until RMS residuals, velocity model, and station terms stabilize. In total, we complete four iterations to achieve the best fitting velocity model (*crust*1) and station corrections (*sta*1). Since Velest does not compute the covariance matrix, the location errors cannot be accurately assessed in this step; therefore, the *crust*1 and *sta*1 data (Figure A3) and absolute traveltimes are again used in Hypoinverse (hereinafter referred to as the *HIb* locations).

A5. The hypoDD Relocation

[45] hypoDD incorporates both differential traveltime and up-sampled cross-correlation delay time data, either individually or combined. Automatic, manual, and cross-correlation delays contribute a varying degree of error to the final relocations. Timing errors of automatically detected arrivals are primarily due to the high SNR ratios, emergent nature of some phases and coda (particularly in the case of *S* wave arrivals of local events) [*Waldhauser and Ellsworth*, 2000]. Typical phase arrival errors for automated picks are 0.1–0.3 s or more. Manually identifying phase arrivals reduces timing errors to ∼0.1 s. Thus, manual phase picking can reduce hypocentral errors from ∼1 km to several hundred meters in the horizontal direction. Vertical hypocentral errors can be up to 2 times larger than horizontal errors due to the difficulty in identifying the *S* wave arrival, either by eye or using an automatic detection algorithm [*Schaff et al.*, 2004]. Employing waveform cross-correlation techniques has been proven to reduce both horizontal and vertical hypocentral errors by 1 to 2 orders of magnitude [*Poupinet et al.*, 1984; *Got et al.*, 1994; *Rubin et al.*, 1999; *Waldhauser et al.*, 1999; *Schaff et al.*, 2002]. Cross correlations increase the precision of the arrival time by exploiting the waveform similarity of nearly colocated events to precisely align up-sampled waveforms. Additionally, since arrival times determined by cross correlations only require the correlation window to be centered on a packet of energy, *S* wave arrivals can be more readily identified even in the case of an emergent arrival or in the presence of *P* wave coda. Up-sampled cross-correlation delay times can thus reduce the timing errors to 0.001 s, which translates to hypocentral errors as small as tens to hundreds of meters.

[46] One critical feature of the algorithm is the complex weighting and reweighting scheme used to incorporate pick information into hypoDD. While the actual weighting values are specific to a given problem, it is generally suggested that for the initial iterations the cross-correlation data should be down-weighted compared to the traveltime data (hereinafter referred to as "catalog data," for consistency with *Waldhauser and Ellsworth* [2000]) and up-weighted in later iterations. The idea is that the catalog data constrain the absolute hypocentral locations at a regional scale, while the cross-correlation data constrain the hypocentral location relative to an event 's neighbors. Each event 's neighbors are selected prior to the relocation in a preprocessing step based on a set of user-defined parameters. hypoDD can be further tailored to the event and station distribution in a specific region by adjusting a variety of parameters.

[47] Since hypoDD only finds relative locations, appropriate steps must be taken to first determine the absolute location of the event, such as the Hypoinverse and Velest procedures described above. For example, running hypoDD with an inappropriate velocity model will move the entire

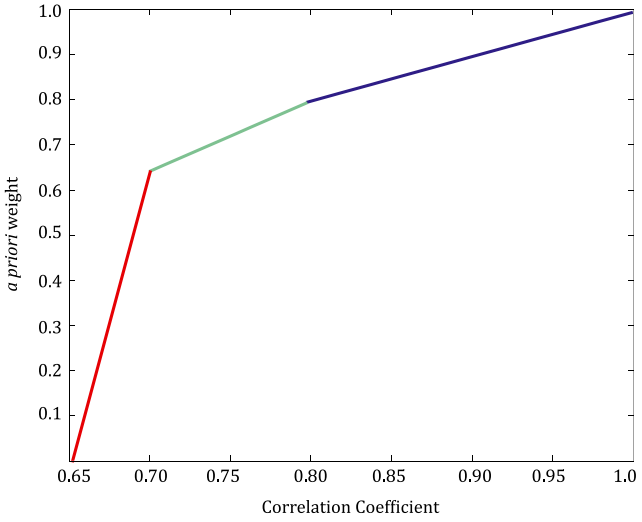

Figure A4. Three empirically derived linear relationships between correlation coefficient (CC) and a priori weight assignment for *P* waves and *S* waves. Events with correlation coefficients below 0.7 have been severally down-weighted (red curve), while events with CC values between 0.7 and 0.8 have only been slightly down-weighted (teal curve). Events with the most similarity (i.e., CC greater than 0.8) retain their CC value (blue curve).

cluster of events in a direction related to the velocity perturbation (i.e., for an overly fast velocity model, the cluster gets pushed farther away from the array). In these situations, the relative location of one event compared to its neighbors remains unaffected, but the absolute locations (and their associated errors) can change dramatically.

[48] The first round of processing incorporates manually picked *P* and *S* wave arrival times for events cataloged by the SCSN and automatic picks for events detected within the UC-RAMP continuous data. The *HIb* results are taken as the starting locations, and we use *crust*1 velocity model with the previously determined V_p/V_s = 1.68. We search for the 10 closest neighbors within a 2 km radius of each event, where each event must be recorded by a minimum of four stations. This process resulted in 405,845 *P*-phase and 251,109 *S*-phase differential times. During relocation, *P* and *S* wave phases that did not meet residual and event-pair separation distance cutoffs were down-weighted. The residual and event-pair separation distance cutoffs were decreased after every second iteration. Residual and distance cutoffs decrease from 8 to 4 s and 6 to 3 km, respectively, over four sets of two iterations. We refer to the results of this first round of hypoDD as *HDa* locations.

[49] Next, we determine cross-correlation delay times and incorporate them into the relocations. For events in the SCSN catalog, the cross correlation is computed on an 0.8 s window around both seismic wave phases; we center the window on the manually picked *P* wave arrival (i.e., 0.4 s before and after the arrival) but include only 0.2 s before the manually picked *S* wave arrival to avoid correlating *P* wave coda. For automatically detected picks, we first employ a station correction method to ensure that the selected window contains the phase energy. Theoretical traveltimes are computed for each event-station pair based on the predicted *TauP* model. Residuals for each station are determined by comparing the manual picks and the theoretical arrival times for events recorded at a given station. The cross-correlation window is shifted by subtracting the residual from the theoretical arrival times estimated from the *HDa* locations. The *P* and *S* wave windows are again taken to be 0.8 s long.

[50] The number of correlations computed is dependent on the number of events, stations, phases, and components considered $(N \times (N-1) \times S \times \mathrm{Ph} \times C/2$; where N = number of events, S = number of stations, Ph = number of phases, and C = number of components), so the number of correlations performed can increase very rapidly ($> 10^9$ calculations). We minimize the number of calculations and the amount of computing time needed to run the cross correlations by restricting the number of correlating events (i.e., neighbors). Using the *HDa* locations, we determine the closest neighbors within a 1 km volume for each target event. Nearly 4 million cross correlations are performed for *P* and *S* wave phases on the vertical and north components of the 13 stations, respectively. The cross-correlation delay times are weighted based on the correlation coefficient and an empirically derived weighting scheme (Figure A4). Only event pairs with cross-correlation coefficients higher than 0.7 are retained. The final results of hypoDD that incorporate differential traveltime and up-sampled cross-correlation delay time data are referred to as *HDb* locations.

Appendix B: Relocation Results

B1. Hypoinverse Results (*HIa* Locations)

[51] We locate 17,465 earthquakes with Hypoinverse using both automated and manually identified phase arrivals from both the SCSN and UC-RAMP. The 4073 events with manual phase detections (hereinafter referred to as the "*HIa*" locations) are shown in Figure 2a. Note that in Figure 2a–2c only events reported in the SCSN catalog for which we manually identified phase arrivals are shown. Errors and residuals will be reported for the entire data set including events reported in the SCSN catalog and those identified in the UC-RAMP continuous data. The absolute horizontal and vertical location errors of the *HIa* locations were reduced to 1.59 km and 2.3 km, respectively, with a RMS residual of 0.25 s. This represents only a marginal improvement over the original SCSN locations (i.e., 1.89 km horizontally, 2.8 km vertically, and RMS of 0.36 s). The majority of the improvement is seen in the vertical error and RMS residual, which we attribute to better *S* wave arrival picks and a slightly improved velocity model. When comparing the two sets of locations, the *HIa* locations form a tighter cluster which is shifted approximately ~1 km to the northeast, which is an effect of the velocity model. These locations remain cloud-like; therefore, identification of fine-scale fault features is not feasible. The locations can be improved by employing a more appropriate velocity model for the region and station terms that account for shallow velocity heterogeneities, as we show below.

B2. Velest Results and Absolute Locations (*HIb* Locations)

[52] We use Velest to determine the best fit velocity model (*crust*1; 10-layer velocity model) and station corrections

(*sta*1) for the available station distribution and earthquakes. The *crust*1 model closely resembles the velocity structure determined in a refraction study by *Fuis and Kohler* [1984] and includes very low seismic velocities in upper the 3 km that reflects the deep sedimentary basin. We compute the station terms with respect to reference station MLDN. Station terms from the joint inversion result in mostly negative site terms but are spatially variable. Station terms are given in Figure A3 and are similar in amplitude to site corrections typically observed for stations located in sedimentary basins [*Richards-Dinger and Shearer*, 2000]. Previous studies have shown that station corrections tend to be positive for soft rock or sedimentary sites and negative for bedrock or basement sites, with similar corrections for nearby sites [e.g., *Richards-Dinger and Shearer*, 2000]. The nonuniform distribution of fast and slow station corrections suggests that the length scale of the velocity heterogeneity in the Yuha Desert is quite small, as is supported by the complex geology detailed by *Isaac* [1987].

[53] A second iteration of Hypoinverse is required after Velest in order to accurately estimate the hypocentral errors associated with the locations. In this step, the absolute phase arrival times are combined with the *crust*1 velocity model and *sta*1 station corrections to invert for absolute locations (labeled *HIb* in Figure 2b). After the Hypoinverse and Velest procedures, the resulting hypocenters have absolute horizontal and vertical location errors of 0.55 and 1.8 km, respectively, with a RMS residual of 0.13 s. Following these steps, the aftershocks begin to "collapse" into linear features resembling faults. These features appear to trend predominantly toward the northwest, with smaller features trending northeast. The most prominent NW striking feature lies slightly east of, but parallel to, the LS-E. Obvious NE striking features lie at the northwestern end of the mapped extensions of the LS-E and LS-W faults. In a 3-D view, planar features that trend northwest parallel to the LS-E and toward the northeast can be identified. Aftershocks in the area north and between stations MLDN and SGL have begun to collapse slightly when compared to the *HIa* locations; however, it is still difficult to discern clear lineations or planar features. Seismicity is still cloud-like and does not form sharp lineations, even after incorporating the best fitting 1-D velocity model and station corrections.

B3. The hypoDD Results (*HDa* and *HDb* Locations)

[54] To further improve the results, we use the *HIb* hypocenter results and *crust*1 velocity model as input in the relative relocation process hypoDD. For the 14,118 events relocated in this step (*HDa* locations), 83% of the original pick data are preserved and the RMS residual is reduced to 0.018 s. Mean horizontal and vertical errors are estimated to be ∼130 and ∼360 m, respectively, through a bootstrap test.

[55] The final relocation step using the *HDa* locations as starting locations combines both the manually and automatically picked traveltimes (404,090 *P*-phase and 251,610 *S*-phase differential times), 1,629,485 *P*-phase and 1,511,309 *S*-phase cross-correlation delay times, and the *crust*1 velocity model. The final locations of the 3540 events recorded by the SCSN with manual picks (*HDb*) are shown in Figure 2c. The errors and residuals of this subset of event locations are marginally better than the entire data set (i.e., 20 m horizontally and 80 m vertically, with a RMS residual of 4 ms). And the locations are consistent with the relocations of Southern California seismicity completed by *Hauksson et al.* [2012]. After all of the relocation steps, there are 9770 relocated events in the study area (shown in Figure 2) with errors of ∼40 m horizontally and ∼120 m vertically, estimated from bootstrap tests. Aftershocks occur as shallow as ∼2 km depth, consistent with the refraction study of *Fuis and Kohler* [1984] showing sedimentary units in the Salton Trough and surrounding region extend to depths between 3 and 4 km.

[56] **Acknowledgments.** We are very grateful to J.H. Steidl and the groups from UCR, UCSB, and CSUSD who participated in the temporary deployment. We further thank J.H. Steidl and W. Ellsworth for their constructive reviews and guidance; our discussions were instrumental to the successful relocation of these earthquakes and clarity of this paper. We highly appreciate J.H. Dieterich's insight and contribution to the aftershock rate section and G.J. Funning's comments on original thesis, from which this work stemmed. Additionally, we thank T. Diehl for sharing useful data reformatting scripts that convert between Velest and hypoDD. The majority of the figures in this paper were made using Generic Mapping Tools (GMT) [*Wessel and Smith*, 1998]. Funding for this work was provided by the Southern California Earthquake Center (SCEC).

References

Antolik, M., R. E. Abercrombie, and G. Ekström (2004), The 14 November 2001 Kokoxili (Kunlunshan), Tibet, earthquake: Rupture transfer through large extensional step-over, *Bull. Seism. Soc. Am.*, *94*, 1173–1194.

Bilham, R. (1989), Surface slip subsequent to the 24 November 1987 Superstition Hills, California, earthquake monitored by digital creepmeters, *Bull. Seism. Soc. Am.*, *79*, 424–450.

Bormann, P. (2012), *New Manual of Seismological Observatory Practice (NMSOP-2)*, IASPEI, GFZ German Research Centre for Geosciences, Potsdam, German, doi:10.2312/GFZ.NMSOP-2.

Bozkurt, E., and A. Koçyiôit (1996), The Kazova basin: An active negative flower structure on the Almus Fault Zone, a splay fault of the system of the North Anatolian Fault Zone, Turkey, *Tectonophysics*, *256*, 239–254.

Chaiarabba, C., and A. Frepoli (1997), Minimum 1D velocity models in central and southern Italy: A contribution to better constrain hypocentral determinations, *Annals of Geophysics*, *40*, 937–954.

Crowell, J. C. (1978), *What We Know and Do Not Know About the History of the San Andreas Fault: Conference on Earth and Space*, University of California, Los Angeles.

Dibblee, T. W. J. (1954), Geology of the Imperial Valley region, California, in *Geology of Southern California: California Division of Mines Bulletin,* vol. 170, edited by R. H. Jahns, pp. 21–28, Calif. Dept. Nat. Res., California.

Dieterich, J. H. (1994), A constitutive law for rate of earthquake production and its application to earthquake clustering, *J. Geophys. Res.*, *99*, 2601–2618.

Dokka, R. K., and R. H. Merriam (1982), Late Cenozoic extension of northeastern Baja California, Mexico, *Geol. Soc. Amer. Bull.*, *93*, 371–388.

Dooley, T. P., and K. R. McClay (1996), Strike-slip deformation in the Confidence Hills, Southern Death Valley Fault Zone, Eastern California, USA, *J. Geol. Soc.*, *153*, 375–387, doi:10.1144/gsjgs.153.3.0375.

Duan, B., and D. D. Oglesby (2006), Heterogeneous fault stresses from previous earthquakes and the effect of dynamics of parallel strike-slip faults, *J. Geophys. Res.*, *111*, B05309, doi:10.1029/2005JB004138.

Fletcher, J. M., T. K. Rockwell, O. Teran, M. E. G. Faneros, K. W. Hudnut, J. Gonzales, A. Gonzalez, R. Spelz, and K. J. Mueller (2010), The surface ruptures associated with the El Mayor-Borrego earthquake sequence, *Geological Society of America*.

Frassetto, A. M., G. Zandt, H. Gilbert, T. L. Owens, and C. H. Jones (2011), Structure of the Sierra Nevada from receiver functions and implications for lithospheric foundering, *Geosphere*, *7*, 898–921, doi:10.1130/GES00570.1.

Freed, A. M. (2005), Earthquake triggering by static, dynamic, and postseismic stress transfer, *Annu. Rev. Earth Planet. Sci.*, *33*, 335–367, doi:10.1146/annurev.earth.33.092203.122505.

Fuis, G. S., and W. M. Kohler (1984), Crustal structure and tectonics of the Imperial Valley region, California, in *The Imperial Basin—Tectonics,*

Sedimentaries, and Thermal Aspects: Pacific Section S.E.P.M, edited by C. A. Rigsby, pp. 1–13, U. S. Geological Survey, Menlo Park, CA.

Got, J. L., J. Fréchet, and F. W. Klein (1994), Deep fault plane geometry inferred from multiplet relative relocation beneath the south flank of Kilauea, *J. Geophys. Res.*, *99*(B8), 15,375–15,386.

Goultry, N. R., R. O. Burford, C. R. Allen, R. Gilman, C. E. Johnson, and R. P. Keller (1978), Large creep events on the Imperial Fault, California, *Bull. Seism. Soc. Am.*, *68*, 517–521.

Hadley, D. M., and H. Kanamori (1977), Seismic structure of the Transverse Ranges, California, *Geol. Soc. Amer. Bull.*, *88*, 1461–1478.

Harding, T. P. (1985), Seismic characteristics and identification of negative flower structures, positive flower structures, and positive structural inversion, *Amer. Assoc. Petro. Geol. Bull.*, *69*, 582–600.

Harding, T. P. (1988), Interpretation of footwall (lowside) fault traps sealed by reverse faults and convergent wrench faults, *Amer. Assoc. Petro. Geol. Bull.*, *72*, 738–757.

Harris, R. A., and S. M. Day (1993), Dynamics of fault interaction: Parallel strike-slip faults, *J. Geophys. Res.*, *98*, 4461–4472.

Harris, R. A., and S. M. Day (1999), Dynamic 3D simulations of earthquakes on en echelon faults, *Geophys. Res. Lett.*, *26*, 2089–2092.

Hauksson, E., and P. Shearer (2005), Southern California hypocenter relocation with waveform cross-correlation, part 1: Results using the double-difference method, *Bull. Seism. Soc. Am.*, *3*(3), 896–903, doi:10.1785/0120040167.

Hauksson, E., L. M. Jones, and K. Hutton (2002), The 1999 M_w 7.1 Hector Mine, California, earthquake sequence: Complex conjugate strike-slip faulting, *Bull. Seism. Soc. Am.*, *92*(4), 1154–1170.

Hauksson, E., J. Stock, K. Hutton, W. Yank, J. A. Vidal-Villegas, and H. Kanamori (2010), The 2010 M_w 7.2 El Mayor-Cucapah earthquake sequence, Baja California, Mexico and southernmost California, USA: Active seismotectonics along the Mexican Pacific margin, *Pure Appl. Geophys.*, *168*, 1255–1277, doi:10.1007/s00024-010-0209-7.

Hauksson, E., W. Yang, and P. M. Shearer (2012), Waveform relocated earthquake catalog for Southern California (1981 to 2011), *Bull. Seism. Soc. Am.*, *102*, 2239–2244.

Helmstetter, A., G. Ouillon, and D. Sornette (2003), Are aftershocks of large Californian earthquakes diffusing?, *J. Geophys. Res.*, *108*(B10), 2483, doi:10.1029/2003JB002503.

Hill, D. P., et al. (1993), Seismicity remotely triggered by the magnitude 7.3 Landers, California, earthquake, *Science*, *260*, 1617–1623.

Hudnut, K. W., and K. E. Sieh (1989), Behavior of the Superstitution Hills fault during the past 330 years, *Bull. Seism. Soc. Am.*, *79*, 304–329.

Hutton, K., E. Hauksson, J. Clinton, J. Franck, A. Guarino, N. Scheckel, D. Given, and A. Yong (2006), Southern California seismic network update, *Seismol. Res. Lett.*, *77*, 389–395.

Isaac, S. (1987), Geology and structure of the Yuha Desert between Ocotillo, California, U.S.A, and Laguna Salada, Baja California, Mexico, Masters thesis, San Diego State University, Calif.

Juliá, J., A. A. Nyblade, R. Durrheim, L. Linzer, R. Gök, P. Dirks, and W. Walter (2009), Source mechanisms of mine-related seismicity, Savuka Mine, South Africa, *Bull. Seism. Soc. Am.*, *99*, 2801–2814, doi:10.1785/0120080334.

King, G. C. P., R. S. Stein, and J. Lin (1994), Static stress changes and the triggering of earthquakes, *Bull. Seism. Soc. Am.*, *84*, 935–953.

Kissling, E., W. Ellsworth, D. Eberhart-Phillips, and U. Kradolfer (1994), Initial reference models in local earthquake tomography, *J. Geophys. Res.*, *99*, 19,635–19,646.

Klein, F. W. (2002), *User's Guide to HYPOINVERSE-2000, a Fortran Program to Solve for Earthquake Locations and Magnitudes*, U.S. Geological Survey, Menlo Park, CA.

Lozos, J. C., D. D. Oglesby, B. Duan, and S. G. Wesnousky (2011), The effects of double fault bends on rupture propagation: A geometrical parameter study, *Bull. Seism. Soc. Am.*, *101*, 385–398, doi:10.1785/0120100029.

Lyons, S. N., Y. Bock, and D. T. Sandwell (2002), Creep along the Imperial Fault, Southern California, from GPS measurements, *J. Geophys. Res.*, *107*, 2249, doi:10.1029/2001JB000763.

Ma, K.-F., and C.-H. Chan (2005), Response of seismicity to Coulomb stress triggers and shadows of the 1999 M_w = 7.6 Chi-Chi, Taiwan, earthquake, *J. Geophys. Res.*, *110*, B05S19, doi:10.1029/2004JB003389.

Magistrale, H., and T. Rockwell (1996), The central and southern Elsinore Fault Zone, Southern California, *Bull. Seism. Soc. Am.*, *6*(6), 1793–1803.

McGill, S. F., C. R. Allen, K. W. Hudnut, D. C. Johnson, W. F. Miller, and K. E. Sieh (1989), Slip on the superstition hills fault and on nearby faults associated with the 24 November 1987 Elore Ranch and Superstition Hills earthquakes, Southern California, *Bull. Seism. Soc. Am.*, *79*, 362–375.

Mendoza, C., and S. H. Hartzell (1988), Aftershock patterns and main shock faulting, *Bull. Seism. Soc. Am.*, *78*, 1438–1449.

Mueller, K. J. (1984), Neotectonics, alluvial history and soil chronology of the southwestern margin of the Sierra de Los Cucapas, Baja California Norte, Master's thesis, San Diego State Univ., San Diego, Calif.

Mueller, K. J., and T. K. Rockwell (1995), Late Quaternary activity of the Laguna Salada fault in northern Baja California, Mexico, *Geol. Soc. Am. Bull.*, *107*(1), 8–18.

Nicholson, C., L. Seeber, P. Williams, and L. R. Sykes (1986), Seismic evidence for conjugate slip and block rotations within the San Andreas fault system, Southern California, *Tectonics*, *4*, 629–648.

Noir, J., S. Békri, P. M. Adler, P. Tapponnier, and G. C. P. King (1997), Fluid flow triggered migration of events in the 1989 Dobi earthquake sequence of central Afar, *Geophys. Res. Lett.*, *24*, 2335–2338.

Ojeda, A., and J. Havskov (2001), Crustal structure and local seismicity in Colombia, *J. Seismolog.*, *5*, 575–593.

Omori, F. (1894), On the after-shocks of earthquakes, *J. Coll. Sci. Tokio Imp. Univ.*, *136*, 111–2000.

Peng, Z., and P. Zhao (2009), Migration of early aftershocks following the 2004 Parkfield earthquake, *Nat. Geosci.*, *2*, 877–881, doi:10.1038/NGEO697.

Perfettini, H., and J.-P. Avouac (2004), Postseismic relaxation driven by brittle creep: A possible mechanism to reconcile geodetic measurements and the decay rate of aftershocks, application to the Chi-Chi earthquake, Taiwan, *J. of Geophys. Res.*, *109*, B02304, doi:10.1029/2003JB002488.

Pinault, C. T., and T. K. Rockwell (1984), Rates and sense of Holocene faulting on the southern Elsinore fault: Further constraints on the distribution of dextral shear between the Pacific and North American plates, *Geol. Soc. Am. Bull. Abstr. Programs*, *16*, 624.

Pontoise, B., and T. Monfret (2004), Shallow seismogenic zone detected from an offshore-onshore temporary seismic network in the Esmeraldas area (northern Ecuador), *Geochem. Geophys. Geosyst.*, *5*, Q02009, doi:10.1029/2003GC000561.

Poupinet, G., W. Ellsworth, and J. Frechet (1984), Monitoring velocity variations in the crust using earthquake doublets: An application to the Calaveras Fault, California, *J. Geophys. Res.*, *89*(B7), 5719–5731.

Ratchkovski, N. A., et al. (2003), Aftershock sequence of the M_w 7.9 Denali fault, Alaska, earthquake of 3 November from regional seismic network data, *Seism. Res. Lett.*, *79*(3), 743–752.

Reasenberg, P., and W. L. Ellsworth (1982), Aftershocks of the Coyots Lake, California, earthquake of August 6, 1979: A detailed study, *J. Geophys. Res.*, *87*, 10,637–10,655.

Richards-Dinger, K. B., and P. M. Shearer (2000), Earthquake locations in Southern California obtained using source-specific station terms, *J. Geophys. Res.*, *105*(B5), 10,939–10,960.

Robinson, D. P., C. Brough, and S. Das (2006), The W_w 7.8, 2001 Kunlunshan earthquake: Extreme rupture speed variability and effect of fault geometry, . *Geophys. Res.*, *11*, B08303, doi:10.1029/2005JB004137.

Rubin, A. M., D. Gillard, and J. L. Got (1999), Streaks of microearthquakes along creeping faults, *Nature*, *400*, 635–641.

Rybicki, K. (1973), Analysis of aftershocks on the basis of dislocation theory, *Phys. Earth. Planet. Inter.*, *7*, 409–422.

Rymer, M. J., et al., (2011), Triggered surface slips in Southern California associated with the 2010 El Mayor-Cucapah, Baja California, Mexico, earthquake, USGS Open-File Report 2010-1333, *Tech. Rep.*

Schaff, D. P., G. H. R. Bokelmann, G. C. Beroza, F. Waldhauser, and W. L. Ellsworth (2002), High resolution image of Calaveras Fault seismicity, *J. Geophys Res.*, *107*(B9), 2186, doi:10.1029/2001JB000633.

Schaff, D. P., G. H. R. Bokelmann, W. L. Ellsworth, E. Zanzerkia, F. Walhauser, and G. C. Beroza (2004), Optimizing correlation techniques for improved earthquake location, *Bull. Seism. Soc. Am.*, *94*(2), 705–721.

Segall, P., and D. D. Pollard (1980), Mechanics of discontinuous faults, *J. Geophys. Res.*, *85*, 4337–4350.

Sharp, R. V. (1967), San Jacinto Fault Zone in the Peninsular Ranges of Southern California, *Geol. Soc. Amer. Bull.*, *78*, 705–730.

Shearer, P. M. (1997), Improving local earthquake locations using the L1 norm and waveform cross correlation: Application to the Whittier Narrows, California, aftershock sequence, *J. Geophys .Res.*, *102*(B4), 8269–8283.

Shearer, P. M., E. Hauksson, and G. Lin (2005), Southern California hypocenter relocation with waveform cross-correlation, part 2: Results using source-specific station terms and cluster analysis, *Bull. Seism. Soc. Am.*, *95*(3), 904–915, doi:10.1785/0120040168.

Smith, A. T., and P. Kasameyer (1997), *Microseismicity Study of the El Hoyo-Monte Galan Geothermal Prospect, Nicaragua*, Lawrence Livermore National Laboratory, Livermore, Calif.

Sumy, D. F., J. B. Gaherty, W.-Y. Kim, T. Diehl, and J. Collins (2013), The mechanics of earthquakes and faulting in the Gulf of California, *Bull. Seism. Soc. Am.*, *103*, 487–506.

Tajima, F., and H. Kanamori (1985), Global survey of aftershock area expansion patterns, *Phys. Earth. Planet. Inter.*, *40*, 77–134.

Thio, H. K., and H. Kanamori (1996), Source complexity of the 1994 Northridge earthquake and its relation to aftershock mechanisms, *Bull. Seism. Soc. Am.*, *86*, S84–S92.

Toda, S., and S. Matsumura (2006), Spatio-temporal stress states estimated from seismicity rate changes in the Tokai region, central Japan, *Tectonophysics*, *417*, 53–68, doi:10.1016/j.tecto.2005.08.030.

Toda, S., R. S. Stein, K. B. Richards-Dinger, and S. B. Bozkurt (2005), Forecasting the evolution of seismicity in Southern California: Animations built on earthquake stress transfer, *J. Geophys. Res.*, *110*, B05S16, doi:10.1029/2004JB003415.

Toda, S., R. S. Stein, V. Sevilgen, and J. Lin (2011), Coulomb 3.3 graphic-rich deformation and stress-change software for earthquake, tectonic, and volcano research and teaching—User guide, *U.S. Geological Survey Open-File Report*, *1060*, 63.

Wald, L. A., and S. Scharwz (2000), The 1999 Southern California Seismic Network bulletin, *Seismol. Res. Lett.*, *71*, 422.

Wald, L. A., L. K. Hutton, and D. D. Given (1995), The Southern California Network bulletin: 1990–1993 summary, *Seismol. Res. Lett.*, *66*, 9–19.

Waldhauser, F., and W. L. Ellsworth (2000), A double-difference earthquake location algorithm: Method and application to the Northern Hayward fault, California, *Bull. Seism. Soc. Am.*, *90*(6), 1353–1368.

Waldhauser, F., and M. Tolstoy (2011), Seismogenic structure and processes associated with magma inflation and hypdrothermal circulation beneath the East Pacific Rise at 9°50′N, *Geochem. Geophys. Geosyst.*, *12*, Q08T10, doi:10.1029/2011GC003568.

Waldhauser, F., W. L. Ellsworth, and A. Cole (1999), Slip-parallel seismic lineations along the northern Hayward fault, California, *Geophys. Res. Lett.*, *26*, 3525–3528.

Wei, S., et al. (2011), Superficial simplicity of the 2010 El Mayor-Cucapah earthquake of Baja California in Mexico, *Nat. Geosci.*, *4*, 615–618, doi:10.1038/NGEO1213.

Weldon II, R. J., T. E. Fumal, T. J. Powers, S. K. Pezzopane, K. M. Scharer, and J. C. Hamilton (2002), Structure and earthquake offset on the San Andreas Fault at the Wrightwood, California, Paleoseismic Site, *Bull. Seism. Soc. Am.*, *92*, 2704–2725.

Wesnousky, S. G. (2006), Predicting the endpoint of earthquake ruptures, *Nature*, *444*, 358–360, doi:10.1038/nature05275.

Wessel, P., and W. H. F. Smith (1998), New, improved version of the Generic Mapping Tools released, *Eos Trans. AGU*, *79*, 579–579.

Yang, W., E. Hauksson, and P. M. Shearer (2012), Computing a large refined catalog of focal mechanisms for Southern California (1981–2010): Temporal stability of the style of faulting, *Bull. Seism. Soc. Am.*, *102*, 1179–1294.